Journal of Materials Chemistry A

Accepted Manuscript

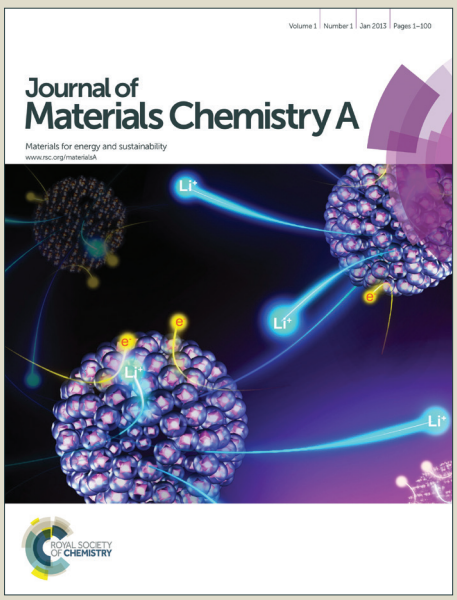

ROYAL SOCIETY OF CHEMISTRY

www.rsc.org/materialsA

Photofuel cell comprising titanium oxide and bismuth oxychloride ($BiO_{1-x}Cl_{1-y}$) photocatalysts for use of acidic water as a fuel†

Yukiko Fujishima,[a,b,#] Seiji Okamoto,[a,#] Mao Yoshiba,[a,#] Takaomi Itoi,[c] Shogo Kawamura,[a] Yusuke Yoshida,[a] Yuta Ogura,[a] and Yasuo Izumi[a,*]

[a] *Department of Chemistry, Graduate School of Science, Chiba University, Yayoi 1-33, Inage-ku, Chiba 263-8522, Japan.*

[b] *Department of Chemistry, Faculty of Science, Tokyo University of Science, Kagurazaka 1-3, Shinjuku-ku, Tokyo 163-8601, Japan.*

[c] *Department of Mechanical Engineering, Graduate School of Engineering, Chiba University, Yayoi 1-33, Inage-ku, Chiba 263-8522, Japan.*

* *E-mail address*: yizumi@faculty.chiba-u.jp, *FAX*: +81-43-290-2783, *Phone*: +81-43-290-3696.

# These authors contributed equally to this paper.

Abstract

Solar and fuel cells have been extensively investigated. However, the need for sustainability, durability, and an electromotive force greater than 1.5 V per cell has not yet been fully satisfied. Herein, a photofuel cell (PFC) utilizing two photocatalysts of TiO_2 and BiOCl for using acidic water as a fuel is described. The PFC is designed such that water can be regenerated from the photogenerated O_2 in the cell, and the electromotive force is as high as the difference between the conduction band minimum of TiO_2 and the valence band maximum of BiOCl (theoretical: 2.75 V, experimental: 1.76 V). The photocurrents were in accordance with a kinetic model based on the combination of the excited electron concentration at TiO_2 and the hole concentration at BiOCl. The reaction of surface sites of O and/or Cl-deficient $BiO_{1-x}Cl_{1-y}$ species formed following ultraviolet–visible light irradiation with O_2 was in-situ monitored using Bi L_3-edge extended X-ray absorption fine structure and X-ray photoelectron spectroscopy supported by Raman and UV-visible spectroscopy and could be involved in cathodic O_2 photoreduction in the PFC. Furthermore, amorphous-like $BiO_{1-x}Cl$ species were observed on the surface of BiOCl crystallines in high-resolution transmission electron microscopy. Importantly, this PFC comprising TiO_2 and BiOCl is sustainable, recyclable, has a series resistance that can be controlled by adjusting the BiOCl particle size, and exhibits a more efficient charge flow because of band bending than that of a previously reported PFC based on rectification of the Schottky barrier.

1 Introduction

Fossil fuels have been utilized as the essential energy source for industrialization. Industrial CO_2 emissions have, however, led to an increase in the atmospheric CO_2 concentration (400 ppm), and the effects of this increase in terms of global warming cannot be underestimated. The development of renewable energy as a replacement for fossil fuels has been slow.[1,2] Among these renewable energies, solar energy has the greatest potential; the solar energy that reaches the earth in 1 h is equivalent to the energy consumed on earth in 1 year.[1,2] Although silicon solar cells (Si SCs) have been commercialized, achieving the widespread adoption of technologies that convert solar energy to electricity often requires government subsidies.[3] Other types of SCs, including compound semiconductors and dye-sensitized SCs,[4] and fuel cells (FCs) that use hydrogen as a fuel,[5] which potentially can be generated using solar energy,[6] have also been extensively investigated. However, all of the requisites (sustainability, durability, and an electromotive force greater than 1.5 V per cell) have not yet been fully satisfied.

Recently, a new device, a photofuel cell (PFC) consisting of the two photocatalysts TiO_2 and silver-doped TiO_2 on an electrode film both immersed in acidic water and separated by a proton-conducting polymer (PCP), was demonstrated.[7] The Schottky barrier between the TiO_2 and Ag nanoparticles at the cathode rectified the cell currents. In the present study, n-TiO_2 and p-BiOCl[8] were used as the anode and cathode, respectively, to enhance the photocurrent generation in the PFC by facilitating charge transfer at the interface between the photocatalyst film and the substrate in the acidic solution. The energy diagram and electron flow in the PFC comprising TiO_2 and BiOCl photocatalysts at pH 2 (typical conditions for PFC tests) is shown in Scheme 1. The energy of the bottom of the conduction band (CB) is −0.41 V @ pH 7 for TiO_2[9] and −1.1 V @ pH 6.8 for BiOCl,[10] whereas the band gap values

for anatase- and rutile-type TiO_2 and BiOCl are 3.2, 3.0,[11,12] and 3.46 eV[13] (Fig. 1A-a), respectively.

The charges in the semiconductors are separated because of ultraviolet (UV) and minor visible light irradiation. The holes in n-TiO_2 are likely to diffuse to the surface to photooxidize water, whereas the electrons in p-BiOCl are likely to diffuse to the surface to photoreduce O_2 molecules because of band bending at the interface (Scheme 1).[14,15] Consequently, electron flow from the CB of TiO_2 to the holes in the valence band (VB) of BiOCl should become predominant with an external circuit. The theoretical electromotive force for the system is 2.75 V (Scheme 1) when any overvoltage due to the carrier level of the electrodes, charge recombination in the photocatalysts, and reverse electron flow from the cathode to anode is not considered. In addition, the use of acidic water as "a fuel" is inexpensive and sustainable. It should be mentioned that acidic water was not exact "fuel" consumed in FCs, but regenerative medium to transfer the charge.[7]

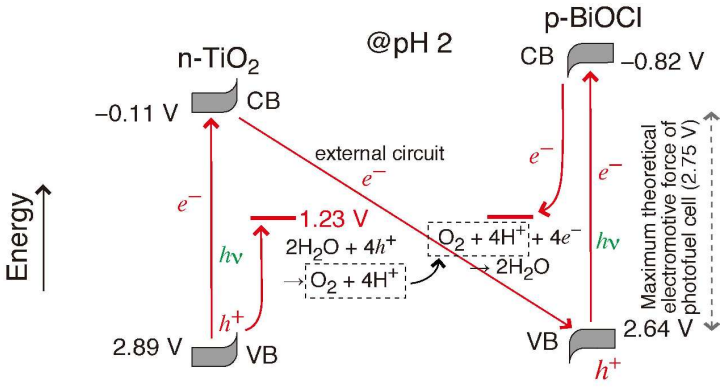

Scheme 1 Energy diagram and electron flow for a PFC comprising TiO_2 and BiOCl.

The PFC in this study was also compared to *photoelectrochemical electrolysis (*or *photoelectrocatalytic) cells* (PECs) already known in the literature (Scheme 2).[16–33] Type 1 PECs consist of a photoanode, e.g., TiO_2 and WO_3, a [photo]cathode, and a redox mediator, e.g., S^{2-}/S_n^{2-} [16] and $Fe^{2+/3+}$,[17] to diffuse the electrons from the cathode to the anode. Type 2 PECs are FCs that consist of a photoanode for fuel oxidation and a conventional cathode,

e.g., Pt–carbon, for O_2 reduction.[18–23] The photoanode and cathode are separated by a PCP film. Type 3 PECs (or *tandem photolysis cells*) consist of a photoanode and a [photo]cathode to form O_2 and H_2, respectively, from water.[23–27] In the cells, a redox mediator is used to diffuse electrons;[28,29] alternatively, protons diffuse from the anode to the cathode if a redox mediator is not employed.[30,31] Type 4 PECs consist of a photoanode to oxidize a fuel (not water) and a photocathode to reduce protons.[32,33]

In summary, PFCs photooxidize water over a photoanode similar to Type 3 PECs and reduce O_2 over a photocathode similar to Type 2 PECs and other FCs. Thus, the specific point of a PFC is the photocatalytic reduction of O_2 at the cathode, which is in contrast to PEC Types 1–4 (Scheme 2).

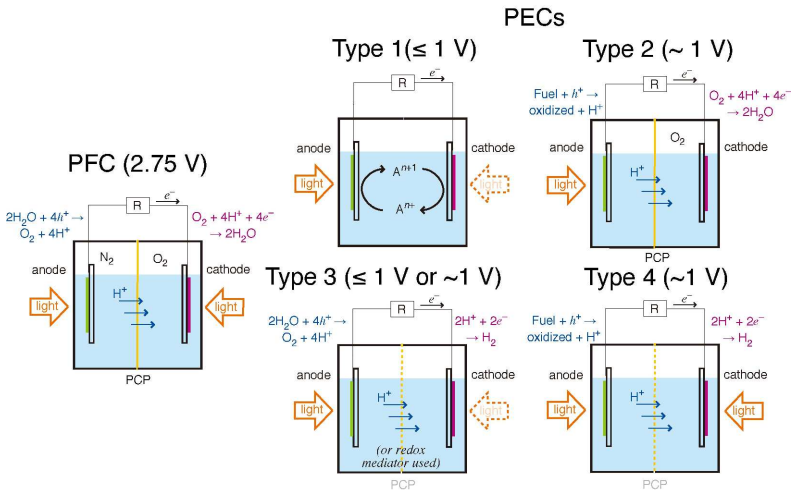

Scheme 2 Components and chemical reactions in a PFC and Type 1–4 PECs. The dotted arrow indicates the possible use of a photoelectrode or a general electrode, and the dotted line at the middle of the cell indicates the possible use of a PCP for separation.

Importantly, the combination of a photoanode and a photocathode in a PFC enables a theoretical electromotive force of as high as 2.75 V (Scheme 1). In Type 1 PECs, the difference (~1 V) between the CB minimum of the photoanode and the potential of the redox mediator is the electromotive force.[30,32] In Type 2 PECs, the difference (~1 V) between the

CB minimum of the photoanode and the electric potential of O_2 reduction is the electromotive force. In Type 3 PECs, the difference between the CB minimum of the photoanode and the VB maximum of the photocathode is the electromotive force if a redox mediator (IO_3^-/I^-, $Fe^{3+/2+}$, Br_2/Br^-)[28,29] is not used.[30] Finally, in Type 4 PECs, the difference between the CB minimum of the photoanode and the VB maximum of the photocathode is the electromotive force. However, the electromotive force is less than 1 V when deep (positive) potential anodic WO_3 and high (negative) potential cathodic Cu_2O are used as photocatalysts for selective oxidation of the fuel and selective reduction of protons, respectively.[33]

A PFC is also different from a dye-sensitized SC, which consists of a dye on a semiconductor and a conventional cathode.[4] The difference (~1 V) between the CB minimum of the photoanode and the potential of the redox mediator is the electromotive force in these systems.

Therefore, the electromotive force between the CB minimum of the photoanode and the VB maximum of the photocathode is advantageous for PFCs and Type 3 and 4 PECs (Scheme 2), but the potential for the reaction $2H^+ + 2e^- \rightarrow H_2$ (0 V @ 298 K & pH 0) in PECs requires a more negative voltage for the CB of the photocathode compared to the voltage (1.229 V @ 298 K, pH 0) required for the reaction $O_2 + 4H^+ + 4e^- \rightarrow 2H_2O$ in a PFC. Consequently, for Type 3 and 4 PECs, the voltage of the VB maximum of the photocathode is more negative, and the difference (electromotive force) with respect to the CB minimum for the photoanode decreases (Scheme 2). Moreover, the reactions in a PFC are completely reversible, allowing the regeneration of water; thus, PFCs are recyclable (Scheme 1).

2 Experimental

2.1 Sample syntheses and preparation of the photoelectrodes

TiO_2 powder [1.00 g; P25, Degussa; anatase/rutile phases = 7/3; Brunauer-Emmett-Teller (BET) surface area (S_{BET}) = 60 m^2 g^{-1}] was suspended in 3.0 mL of deionized water (<0.06 μS cm^{-1}) and then stirred well. The obtained suspension was dried at 373 K for 24 h and heated in air at 673 K for 2 h. The resultant powder was suspended in 75 μL of deionized water and placed on an indium tin oxide (ITO, thickness 1.2–1.6 μm)-coated Pyrex glass plate. The TiO_2/ITO/Pyrex was dried at 373 K for 18 h and heated in air at 573 K for 30 min. The amount of TiO_2 deposited on the ITO-coated glass plate was 5.0 mg and covered an area of 1.3 cm^2.

BiOCl was synthesized using a solvothermal procedure.[34] Bismuth nitrate pentahydrate (2.00 g; >99.5%, Wako Pure Chemical) was dissolved in 80 mL of ethylene glycol (>99.5%, Wako Pure Chemical), and then cetyltrimethylammonium chloride (1.30 g; >95%, Wako Pure Chemical) was added to the mixture. The solution was magnetically stirred at a rate of 900 rotations per minute (rpm) at 290 K for 1 h. Next, an ethene glycol solution (4.5 mL) of potassium hydroxide (1.0 mol L^{-1}; 85%, Wako Pure Chemical) was added. The solution was then introduced into a Teflon-lined autoclave (Model TVS-N2-100, Taiatsu Techno) and maintained at 433 K for 12 h. This solution was filtered using a polytetrafluoroethene membrane filter (Model Omnipore JGWP04700, Millipore) with a pore size of 0.2 μm, and the collected white powder was washed with deionized water (total 450 mL) and ethanol (total 450 mL) and dried at 323 K for 12 h. The obtained white BiOCl powder is denoted as solvo-BiOCl (or simply BiOCl).

For comparison, some of the experiments were also performed using BiOCl synthesized from an aqueous solution.[35] For this process, 3.15 g of Bi trichloride (>97%; Wako Pure Chemical) was dissolved in 100 mL of deionized water. The solution was agitated using ultrasound (430 W, 38 kHz) for 10 min and then magnetically stirred at 290 K in the dark for

2 h. The precipitate was filtered using a JGWP04700 filter, washed with ethanol (total 200 mL), and dried at 353 K for 12 h. The obtained BiOCl is denoted as aqua-BiOCl.

The obtained BiOCl powders (solvo-BiOCl and aqua-BiOCl) were each suspended in 38 μL of deionized water and placed on ITO-coated glass plates in a manner similar to that used for the TiO_2/ITO/Pyrex. The amount of BiOCl placed on each ITO-coated glass plate was 2.5 mg and covered an area of 1.3 cm^2.

2.2 Characterization

Optical spectroscopic measurements were performed using a UV–visible spectrophotometer (Model V-650, JASCO) with D_2 and halogen lamps for wavelengths below and above 340 nm, respectively. An integrating sphere (Model ISV-469, JASCO) was used for the diffuse reflectance (DR) measurements. The samples were placed in contact with the quartz window glass in a gas-tight DR cell (photographs in Scheme 3), and the interior atmosphere was either argon or air. Measurements were performed at 290 K within the wavelength range of 200–800 nm using 200 mg of the sample. The DR spectra were converted to absorption spectra using the Kubelka–Munk equation.[36,37] The band gap value was estimated via simple extrapolation of the absorption edge or by fitting to the Davis–Mott equation:

$$\alpha \times h\nu \propto \left(h\nu - E_g\right)^n \qquad (1),$$

where α, h, and ν are the absorption coefficient, Planck's constant, and frequency of light, respectively, and n is 1/2, 3/2, 2, or 3 for the allowed direct, forbidden direct, allowed indirect, and forbidden indirect electronic transitions, respectively.[38]

High-resolution transmission electron microscopy (HR-TEM) images were observed using a Titan G2 60-300 (FEI) field emission-type transmission electron microscope

operating at 300 kV. The HR-TEM video images were observed using a JEM-2100F (JEOL) field emission-type transmission electron microscope operating at 200 kV. The samples were mounted on a conducting carbon-with-Cu grid mesh (100 mesh per inch). The electron currents at the sample position were estimated to be between 500 and 100 pA cm^{-2} on the basis of the counts on a fluorescence plate that was placed at a distance of 76 cm from the sample on the opposite side of the electron source. We observed BiOCl samples after sufficient astigmatism correction using amorphous carbon film in the HR-TEM observation. The intervals of the lattice planes were calculated for tetragonal BiOCl with a = 0.389 1 nm and c = 0.736 9 nm,[39,40] and these were compared to the observed lattice intervals.

X-ray diffraction (XRD) patterns were observed at a Bragg angle of $2\theta_B$ = 10°–70° with a scan step of 0.01° and a scan rate of 4 s per step using a D8 ADVANCE diffractometer (Bruker) at the Center for Analytical Instrumentation, Chiba University. The measurements were performed at 40 kV and 40 mA using Cu Kα radiation and a nickel filter. The sample irradiated with UV–visible light for 9 h under an Ar atmosphere was also analyzed using a gas-tight XRD holder with a semispherical cap (Model A100-B37, Bruker). The mean particle size (t) of the BiOCl was determined using the Scherrer equation

$$t = \frac{0.9\lambda}{\text{Full\_width\_at\_half\_maximum} \cdot \cos\theta_B} \qquad (2).$$

Raman spectra were measured at 290 K using a model NRS-5100 (JASCO) with the excitation wavenumber of 532 nm for the solvo-BiOCl samples as-synthesized and irradiated by UV-visible light for 12 h under vacuum. The intensity of the laser was ~1 mW and a CCD detector was used at 203 K.

X-ray photoelectron spectra (XPS) were measured using a Model AXIS-NOVA, Shimadzu/Kratos equipped with X-ray source Al Kα (1 486.6 eV). O 1s, Bi $4f_{5/2}$, and Bi $4f_{7/2}$ regions were narrow scanned. The C 1s (284.8 eV) was used as a reference for energy

calibration for adventitious hydrocarbon on the specimen surface.[41] BiOCl sample under Ar irradiated by UV-visible light for 2.5 h and another BiOCl sample immersed in HCl aqueous solution (pH 2.0) under O_2 irradiated by UV-visible light for 2.5 h were mounted on sample holder and the sample holder was introduced to a transfer vessel under Ar atmosphere. The transfer vessel was connected to AXIS-NOVA, the gate valve was opened, and then the sample was transferred inside AXIS-NOVA without any contact to air.

Bismuth L_3-edge extended X-ray absorption fine structure (EXAFS) spectra were obtained at 290 K in the transmission mode in the Photon Factory Advanced Ring and Photon Factory at the High Energy Accelerator Research Organization (Tsukuba) on beamlines NW10A and 9C.[42–45] The storage ring energy was 6.5 and 2.5 GeV, and the ring current was 33.0–55.8 and 450 mA. A Si (311) and (111) double-crystal monochromator and a platinum and rhodium-coated focusing cylindrical mirror, respectively, were inserted into the X-ray beam path. The X-ray intensity was maintained at 65% of the maximum flux using a piezo translator attached to the crystal. The slit opening size was 1 mm (vertical) × 2 mm (horizontal) in front of the ionization chamber. The samples were thoroughly mixed with boron nitride and pressed as disks. Some samples were in Pyrex glass cells equipped with polyethene naphthalate film (PEN; Q51-16, Teijin-Dupont; 25 μm thick) windows on both sides, purged with Ar or filled with HCl aqueous solution (pH 2.0) with O_2 gas. The PEN film was transparent for X-rays, visible light, and a portion of the UV light region (>370 nm) and enabled *in situ* monitoring of the photocatalysts.[36,46–49] The Bi L_3-edge absorption energy was calibrated to 13 426 eV for the spectrum of Bi metal.[50]

The EXAFS data were analyzed using an XDAP package.[51] The procedure has been described previously.[36,47,52,53] Multiple-shell curve-fit analyses were performed for the Fourier-filtered k^3-weighted EXAFS data in both k- and R-space using empirical amplitude and phase-shift parameters theoretically generated using FEFF version 8.4[54] for the crystal

structure of Bi metal powder or extracted from the EXAFS data for Bi_2O_3 (>98%, Wako Pure Chemical) and $BiCl_3$ powders. The interatomic distances (*R*) and associated coordination numbers (*N*) for the Bi–Bi, Bi–O, and Bi–Cl pairs were set to 0.307 1 nm with an *N* value of 3, 0.352 9 nm with an *N* value of 3,[55] 0.233 0 nm with an *N* value of 5,[56] and 0.250 0 nm with an *N* value of 3 (Tables 1d, e, and g).[57]

Cyclic voltammetry (CV) measurements were performed for BiOCl as the working electrode (WE) (BiOCl/ITO/Pyrex and a Au/Ni-coated stainless clip; Toyo Corporation), glassy carbon as the counter electrode (CE) (Model 002012, $\phi_{PolyEtherEtherKetone}$: 6.0 mm, ϕ_C: 3.0 mm; BAS Incorporation), and Ag/AgCl as the reference electrode (Model RE-1B, BAS Incorporation), immersed in a hydrochloric acid solution of pH 4.0. The voltage of the WE was swept between −1.22 and 1.50 V versus Ag/AgCl at a rate of 50 mV s^{-1} using a potentio/galvanostat (Model VersaSTAT 3-100, Princeton Applied Research) in either O_2 or N_2 atmosphere at a flow rate of 100 mL min^{-1} irradiated using UV–visible light (8 mW cm^{-2} at the WE sample position) or in the dark.

2.3 PFC Tests

TiO_2/ITO/Pyrex and BiOCl/ITO/Pyrex electrodes were immersed in HCl solutions (40 mL in each compartment; initial pH between 2.0 and 4.0). The two compartments were separated by a 50 μm-thick PCP film (Nafion, DuPont; acid capacity > 9.2×10^{-4} equivalent g^{-1}). N_2 and O_2 gases were bubbled 30 mm away from each photoelectrode at a flow rate of 100 mL min^{-1} (Fig. S1).[7] The PFC was equipped with quartz windows (ϕ = 80 mm) on both sides. Both the TiO_2 and BiOCl photocatalysts were irradiated with UV–visible light through the quartz windows using a two-way branched quartz fiber light guide (Model 5ϕ–2B–1000L, San-ei Electric Co.) from a 500-W xenon arc lamp (Model SX-UID502XAM, Ushio). The

distance between the light exit (ϕ = 5 mm) and the TiO_2 or BiOCl film was 46 mm. The light intensity was 8 mW cm^{-2} at the center of the photocatalyst film on each electrode.

Static photocurrent generation tests were performed by connecting the external parallel circuit for one route via a voltmeter and another route via an ammeter with a resistance of 0.5 Ω (Fig. S1). Both catalysts were exposed for 30 min to UV–visible light and then kept in the dark for 30 min, and this process was typically repeated five times. As a reference, static photocurrent test using TiO_2/ITO/Pyrex and BiOCl/ITO/Pyrex electrodes were immersed in H_2SO_4 and HCl solutions, respectively, both at pH 2.0 was performed. Static photocurrent test exposed to continuous UV-visible light on for 3 h was also performed. The current (i) and voltage (V) between the two electrodes were monitored. The i–V characteristics were also measured using a similar parallel circuit; however, the resistance was gradually varied from 500 kΩ to 0.3 Ω over 20 min.

In comparison, the BiOCl (solvo-BiOCl, aqua-BiOCl) fine powder (0.135 g) was irradiated using UV–visible light for 12 h in a quartz glass reactor[2,36,48,53] under vacuum connected to rotary and diffusion pumps (10^{-6} Pa), and then the reaction with 2.91 kPa of O_2 was monitored by the pressure change using a capacitance manometer (Models CCMT-100A and GM-2001, ULVAC). The rate constant k was determined by fitting to the equation for the first order reaction rate

$$\ln\frac{P_{O_2}-P_{O_2,\text{final}}}{P_{O_2,\text{initial}}-P_{O_2,\text{final}}}=-kt \qquad (3)$$

where $P_{O_2,\text{initial}}$ and $P_{O_2,\text{final}}$ are the initial and final pressures of O_2, respectively.[47]

3 Results

3.1 Characterization of BiOCl

3.1.1 As-synthesized BiOCl

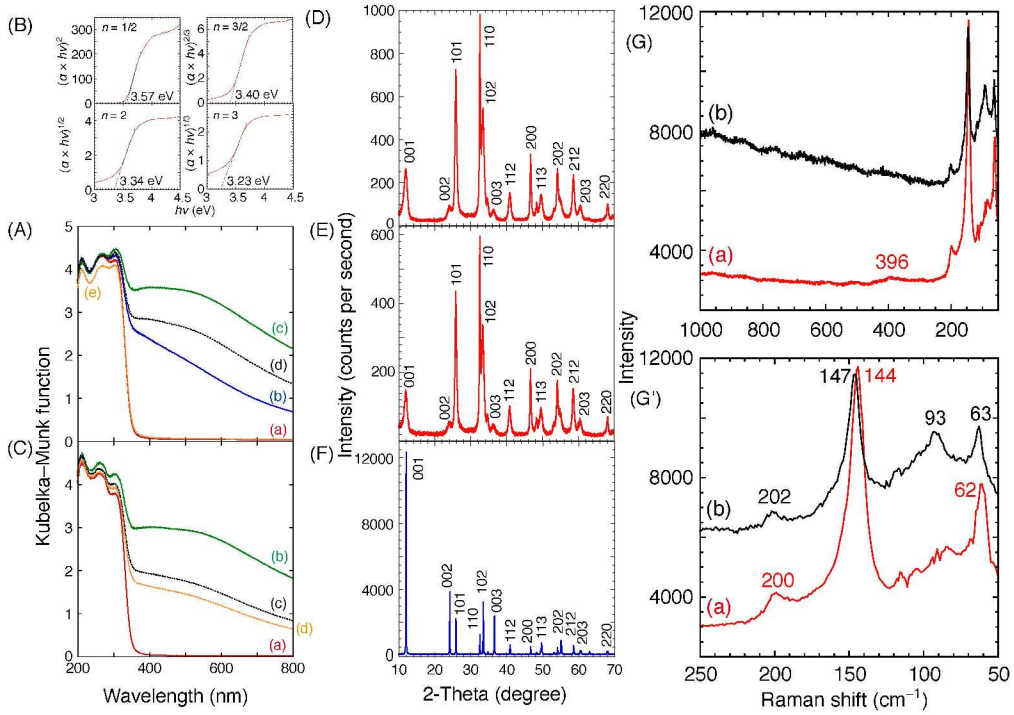

Fig. 1 **(A)** UV–visible absorption spectra for solvo-BiOCl (a) as-synthesized, irradiated under UV–visible light in Ar for (b) 1 min and (c) 1.0 h, (d) sample c in the dark for 24 h, and (e) sample d exposed to air for 5 h. (B) Fitting to the Davis–Mott equation for the data in A-a. The values for $(\alpha \times h\nu)^2$, $(\alpha \times h\nu)^{2/3}$, $(\alpha \times h\nu)^{1/2}$, or $(\alpha \times h\nu)^{1/3}$ versus $h\nu$ were plotted, and the intercept with the *x*-axis estimated the E_g value. **(C)** UV–visible absorption spectra for solvo-BiOCl (a) as-synthesized, (b) irradiated under UV–visible light in air for 1.0 h, and sample b in the dark (c) for 24 h and (d) 92 h. XRD patterns for solvo-BiOCl **(D)** as-synthesized, **(E)** irradiated with UV–visible light under Ar for 9 h, and aqua-BiOCl **(F)** as-synthesized. **(G, G')** Raman spectra for BiOCl (a) as-synthesized and (b) irradiated using UV–visible light for 12 h under vacuum.

Solvo-BiOCl. The UV absorption edge for the as-synthesized BiOCl was simply extrapolated to 358 nm (Fig. 1A-a). The E_g value was evaluated on the basis of the fit to the eq. 1. As shown in the fittings for $(\alpha \times h\nu)^{1/n}$ versus $h\nu$ (n = 1/2, 3/2, 2, and 3; Fig. 1B), the E_g values (3.57–3.40 eV) when n was 1/2 or 3/2 were consistent with that given by simple extrapolation of the absorption edge (3.46 eV) and results reported in the literature (3.46 eV).[13] In fact, when the $\ln(\alpha \times h\nu)$ value was plotted versus $\ln(h\nu - 3.46)$, the n value was

found from the slope to be 1.030. Thus, a direct transition from Cl 3p (and/or O 2p) to Bi 6p was suggested.[58]

The XRD peak position and intensity ratio for the as-synthesized BiOCl (Fig. 1D) were in accordance with those reported in literature.[13,59] The mean particle size of the BiOCl was determined to be 24(±12) nm using the eq. 2. The mean particle size in the (001) direction was smaller (13(±2) nm) compared to mean particle size 40(±13) nm in perpendicular plane to the [001] direction, indicating the disk-like crystalline growth.

Raman spectrum for as synthesized BiOCl was measured (Fig. 1G-a, G'-a). For the tetragonal symmetry of BiOCl,[13] A_{1g}, B_{1g}, and E_g vibration modes were possible for Raman and if we assume the ionic crystal of BiOCl as "molecular" crystal, internal and external vibration modes were considered within and beyond the "molecule", respectively. The peaks at 200, 144, and 62 cm^{-1} were assigned to internal E_g, internal A_{1g} (and minor external E_g), and external A_{1g} for Bi–Cl stretching modes, respectively.[10] The weak peak at 396 cm^{-1} was assigned to E_g and/or B_{1g} modes for the motion of oxygen.

The XP spectrum in the Bi $4f_{5/2}$ and Bi $4f_{7/2}$ regions was measured for as-synthesized BiOCl (Fig. 2A-a). The peaks centered at 164.7 and 159.4 eV, corresponding to Bi^{3+} state of BiOCl.[41] These were consistent with the reported values at 164.4–164.5 and 159.1–159.9 eV,[58,60] respectively, if the C 1s peak energy is assumed to be 284.8 eV.[41]

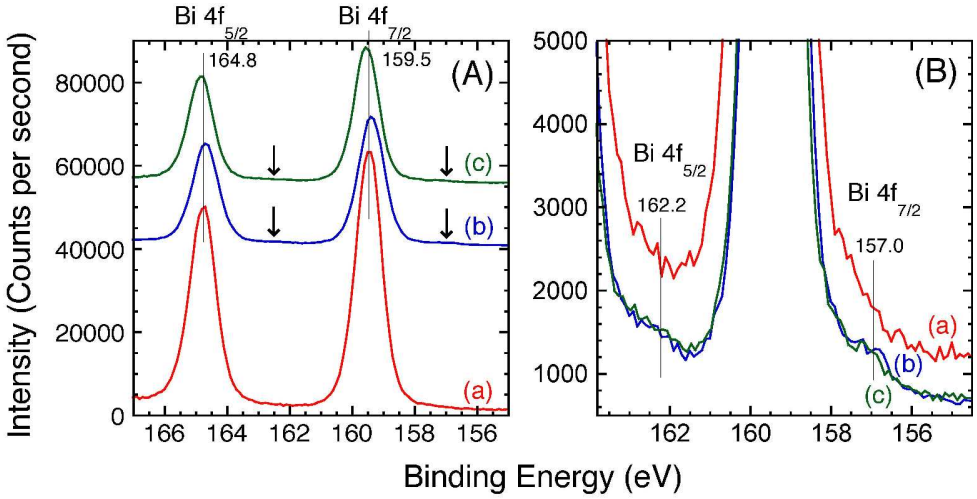

Fig. 2 XPS spectra in the Bi $4f_{5/2}$ and Bi $4f_{7/2}$ regions for as-synthesized BiOCl (a), BiOCl in Ar irradiated by UV-visible light for 2.5 h (b), and BiOCl in HCl aqueous solution with O_2 irradiated by UV-visible light for 2.5 h (c).

The Bi L_3-edge EXAFS curve-fitting analysis for the as-synthesized BiOCl indicated Bi–O and Bi–Cl coordination at 0.244 and 0.307 nm, respectively (Table 1a and Fig. 3a), confirming the synthesis of BiO^+ layers and intercalated Cl^- anions.[13]

From the HR-TEM images of the as-synthesized BiOCl (Fig. 4a), the particle size ranged between 10 and 20 nm, which is nearly in accordance with the mean particle size (24 nm) estimated on the basis of the XRD analysis. Lattice patterns with intervals of 0.33–0.34 nm were assigned to the 011 planes (calculated interval 0.34 nm based on the crystal structure).[39] Lattice patterns with intervals of 0.40 nm were also observed and assigned to the 002 planes (calculated interval 0.37 nm).

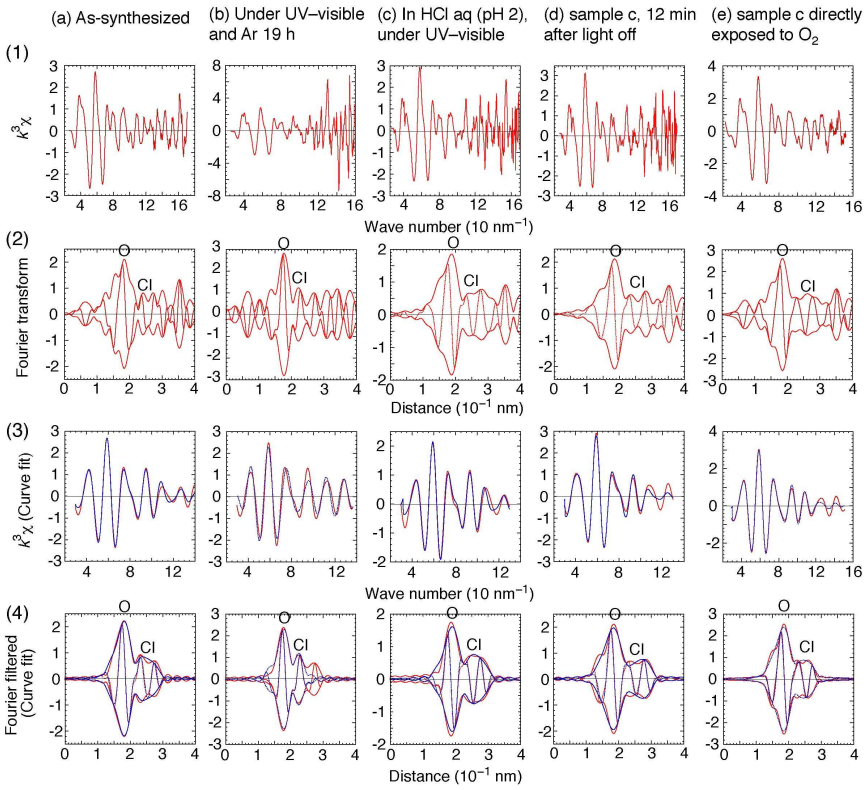

Fig. 3 (**a**) Bi L_3-edge EXAFS spectra for as-synthesized BiOCl, (**b**) sample "a" under Ar and UV–visible light for 19 h, and (**c**) sample "a" immersed in a pH 2.0 HCl solution under O_2 and UV–visible light for 35 min, (**d**) 12 min after UV–visible light was off for sample "c", and (**e**) sample "c" was directly exposed to ambient air. (**1**) k^3-weighted EXAFS χ-function, (**2**) its associated Fourier transform, and best-fit results in **(3)** *k*-space and **(4)** *R*-space to the Fourier-filtered transformed data. The red and blue lines represent the experimental and calculated values, respectively. The solid line represents the magnitude, and the dotted line indicates the imaginary part in panels **2** and **4**.

Table 1 Curve-fitting analysis of the Bi L_3-edge EXAFS results for BiOCl[a]

Sample	Bi–O	Bi–Cl	Bi–Cl	Bi–Bi	Bi–Bi	Goodness of fit
			R (nm)			
			N			
			$\Delta\sigma^2$ (10^{-5} nm^2)			
(a)	0.244 (±0.002)	0.307 (±0.011)				
As synthesized	4.0 (±0.7)	4.0 (±1.7)				3.5×10^4
	2.7 (±5.5)	1.2 (±3.7)				
(b)	0.241 (±0.015)	0.276 (±0.021)				
In Ar & UV-visible, 19 h	1.9 (±0.9)	3.7 (±0.2)				1.6×10^5
	3.3 (±2.5)	5.5 (±1.6)				
(c)	0.250 (±0.001)	0.329 (±0.012)				
In HCl (pH 2.0), O_2 gas, & UV-visible, 35 min	2.2 (±0.2)	3.1 (±0.7)				1.4×10^5
	1.4 (±0.5)	2.2 (±1.7)				
(d)	0.247 (±0.001)	0.331 (±0.012)				
Sample c, 12 min after UV-visible was off	4.2 (±0.6)	4.6 (±1.9)				3.2×10^5
	6.0 (±1.4)	5.7 (±1.8)				
(e)	0.247 (±0.012)	0.301 (±0.009)				
Sample c was directly exposed to air	5.1 (±1.6)	3.1 (±1.7)				
	3.6 (±1.9)	2.2 (±3.6)				
(f) Bi_2O_3 (model)[56]	0.233 0 5 —					
(g) $BiCl_3$ (model)[57]		0.250 0 3 —				
(h) BiOCl[39]	0.231 4 4 —	0.307 1 4 —	0.350 0 1 —			
(i) Bi metal (model)[55]				0.307 1 3 —	0.352 9 3 —	

[a] The values in parentheses are evaluated fit errors

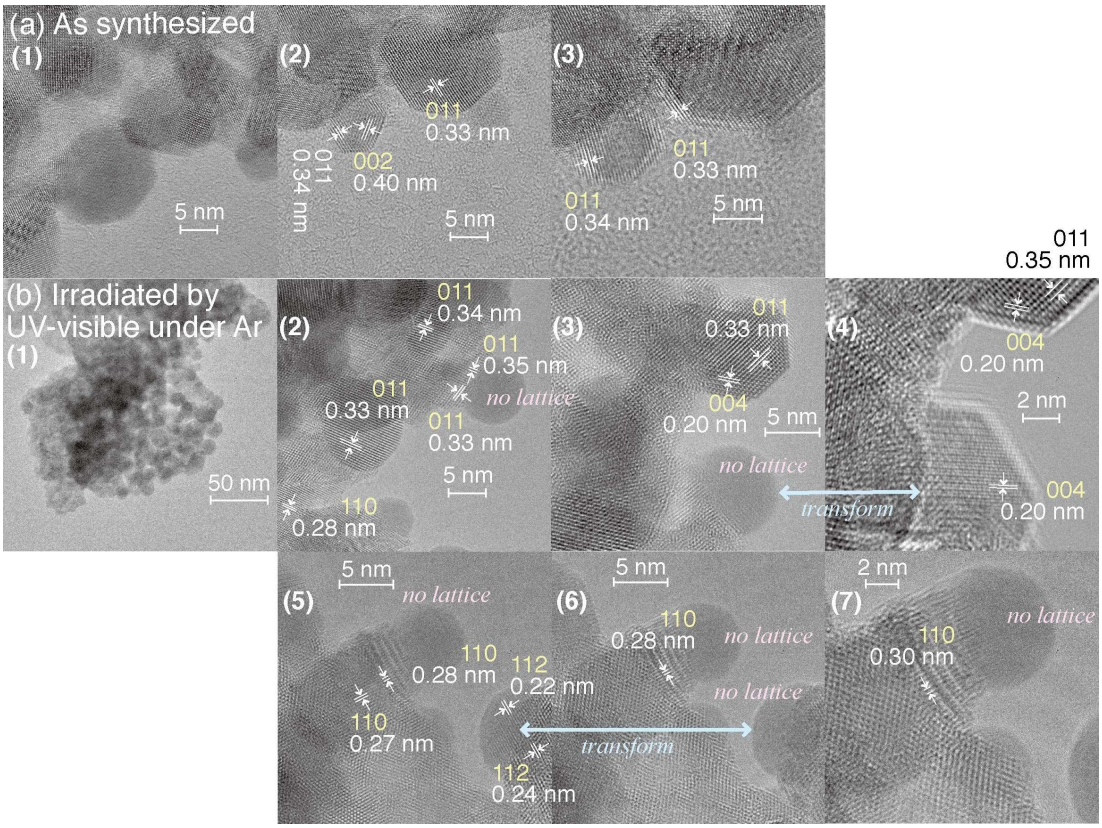

Fig. 4 HR-TEM images observed for the (a) as-synthesized BiOCl and (b) a BiOCl irradiated with UV–visible light for 9 h in an Ar atmosphere.

Aqua-BiOCl. The UV–visible spectrum and XRD peak position obtained for the aqua-BiOCl were similar to those of the BiOCl (Fig. 1D, F); however, the mean particle size was significantly greater at 115(±49) nm, as determined from the XRD peak width. This trend was in accord with literature in which water was hydrolysis agent in contrast to ethene glycol was crystal growth inhibitor during the synthesis of BiOCl.[61] The mean particle size in the [001] direction was greater (168(±28) nm) compared to mean particle size (121(±72) nm) in perpendicular plane to the (001) direction, indicating preferable crystalline growth in the *c*-axis.

3.1.2 BiOCl irradiated under Ar/vacuum

When the BiOCl powder under an Ar atmosphere was irradiated with UV–visible light, the white color changed to brown and the light absorption increased over the entire visible light range in 1 min (Fig. 1A-b). When the irradiation was continued, the color further changed to black (Scheme 3b, photograph) and light absorption enhanced progressively over the entire visible light region for 1 h (Fig. 1A-c).

The black color slowly diminished to gray after 24 h under Ar in the dark (Fig. 1A-d), and the gray color changed negligibly after 5 days under Ar and in the dark, but returned to white within 5 h when the sample was exposed to ambient air. In addition, the UV–visible spectrum of the recovered white sample was essentially identical to that for the as-synthesized BiOCl (Fig. 1A-e). Thus, the species/phase responsible for the black color under Ar and light exposure was reversibly transformed to the original BiOCl crystalline in air.

Raman spectrum for BiOCl irradiated using UV-visible light for 12 h under vacuum was measured (Fig. 1G-b, G'-b). The peaks at 200 (internal E_g), 144 [internal A_{1g} (and minor external E_g)], and 62 cm^{-1} (external A_{1g}) for Bi–Cl stretching modes of as synthesized BiOCl remained almost constant at 202, 147, and 63 cm^{-1}, respectively.[10] Furthermore, a new peak appeared at 93 cm^{-1} (Fig. 1G'-b). A pair of peaks at 95 and 69 cm^{-1} was reported for metallic Bi,[10] however no peak at 69 cm^{-1} appeared in Fig. 1G-b. Therefore, we assume the new peak at 93 cm^{-1} was due to Bi–Cl stretching mode enabled for the black, O-deficient BiOCl.

XP spectrum in the Bi $4f_{5/2}$ and Bi $4f_{7/2}$ regions was measured for BiOCl irradiated by UV-visible light for 2.5 h in Ar atmosphere (Fig. 2A-b). The peaks remained at the same position (164.7 and 159.4 eV) as that for as-synthesized sample (Fig. 2A-a). In addition to the peaks due to Bi^{3+} state, weaker peaks appeared centered at 162.2 and 157.0 eV (arrows in Fig. 2A-b and 2B-b). The two peaks shifted by −2.5 and −2.4 eV compared to corresponding $4f_{5/2}$ and $4f_{7/2}$ peaks due to Bi^{3+}, respectively. Compared to chemical shift for Bi $4f_{7/2}$ peak on

going from $Bi^{III}OCl$ to Bi^0 (3.1 eV),[41] the weaker peaks at 162.2 and 157.0 eV should be derived from reduced Bi sites at the valence between 3 and 0.

Based on the EXAFS analyses, the *N* values for the interatomic Bi–O pair decreased from 4.0 to 1.9 when the as-synthesized BiOCl powder was irradiated under Ar using UV–visible light for 19 h (Table 1a and b and Fig. 3a, b). Conversely, after irradiation, the *N*(Bi–Cl) value only changed slightly from 4.0 to 3.7. Bi atoms that lost neighboring lattice O atoms may have formed shorter bonds with Cl: 0.276 nm compared to 0.307 nm for the original crystalline BiOCl (Table 1a, b). Thus, these results suggested that the generation of O deficiencies in the crystalline BiOCl due to UV–visible irradiation in an Ar atmosphere occurred. The curve fitting to the model function for a metallic Bi–Bi pair was unsuccessful (Fig. 3b).

Even after UV–visible light irradiation in an Ar atmosphere for 9 h, the whole XRD pattern negligibly changed compared to that for the as-synthesized BiOCl (Figs. 1D, E). The mean particle size did not change at 24(±12) nm for as-synthesized BiOCl and one irradiated with UV-visible light under Ar. Thus, following UV–visible light irradiation under an Ar atmosphere, the major phase was crystalline BiOCl, and a minor O-deficient amorphous-like phase resulted in the black color.

An HR-TEM image for BiOCl irradiated with UV–visible light in an Ar atmosphere was obtained (Fig. 4b). Similar to the image for the as-synthesized BiOCl (Fig. 4a), particles with sizes ranging from 10 to 20 nm were observed, and lattice patterns with intervals of 0.33–0.35, 0.20, 0.22–0.24, and 0.27–0.30 nm were assigned to the 011, 004, 112, and 110 planes (calculated lattice intervals of 0.34, 0.19, 0.22, and 0.28 nm, respectively).

During the HR-TEM observation, a portion of the external nanocrystals of BiOCl transformed to spherical nanoparticles without lattices (Fig. 4b3, right, bottom and 3b6, center, right, and bottom; Fig. 4b7 is a zoomed image of 4b6). When the observation was

continued, the amorphous-like spherical nanoparticles transformed back to nanocrystals of BiOCl with a clear lattice pattern (Fig. 4b4, right, bottom and 3b5, right and bottom). This phase transformation was reversible (a video is available as an *Electronic Supplementary Material*). Thus, the amorphous-like spherical nanoparticles were oxygen-deficient $BiO_{1-x}Cl$ that formed under the electron flux of the HR-TEM. The 110 and 112 lattice patterns in Fig. 4b5 (left and right) in the reversibly transformed BiOCl crystals were continuous with the 110 and 112 lattice patterns, respectively, present in the lower, unchanging BiOCl particles. This fact suggests that O atoms were supplied from the lower BiOCl particles to the amorphous-like, oxygen-deficient $BiO_{1-x}Cl$ species to enable crystallization as BiOCl from the boundary toward the $BiO_{1-x}Cl$ nanoparticles.

Thus-observed reversible phase transformation should not be an artifact because the amorphous-like spherical nanoparticles (Fig. 4b3, right, bottom and 3b6, center, right, and bottom, and Fig. 4b7) were rarely observed for the as-synthesized BiOCl (Fig. 4a1–3). The adjustment of astigmatism was sufficient as in the video (*Electronic Supplementary Material*).

3.1.3 BiOCl irradiated under O_2/air and/or HCl aqueous solution

Corresponding to the conditions of PFC tests, the on/off exposure of BiOCl to UV–visible light in air was performed, and the UV–visible absorption spectra were monitored (Fig. 1C). When fresh BiOCl was irradiated with UV–visible light for 1 h, the color changed to black, and its light absorption increased over the entire visible light region (Fig. 1C-b). The absorbance was ~80% of that following irradiation with light for 1 h under Ar (Fig. 1A-c). When the black sample was stored in air in the dark for 24 h, the color faded to gray, and the absorbance was ~65% of that of the corresponding sample stored under Ar in the dark for 24 h (Figs. 1C-c and 1A-d).

In addition, the BiOCl irradiated in air remained gray in the dark, even after 92 h (Fig. 1C-d), which is in clear contrast to the behavior of the BiOCl irradiated under Ar, which completely turned white within 5 h upon exposure to air (Fig. 1A-e). Thus, it can be concluded that the $BiO_{1-x}Cl$ formed when the BiOCl was irradiated in air (or O_2) with UV–visible light was stabilized by outer oxidized layers (Scheme 3e).

XP spectrum in the Bi $4f_{5/2}$ and Bi $4f_{7/2}$ regions was also measured for BiOCl irradiated by UV-visible light for 2.5 h immersed in HCl aqueous solution (pH 2.0) saturated with O_2 (Fig. 2A-c). Although the Bi^{3+} peaks were again predominant at 164.8 and 159.5 eV, weaker peaks appeared centered at 162.2 and 157.0 eV (arrows in Fig. 2A-c and 2B-c) similar to reduced Bi sites at the valence between 3 and 0 for irradiated BiOCl in Ar atmosphere (Fig. 2B-b). The peak intensity of the $4f_{5/2}$ and $4f_{7/2}$ peaks for reduced Bi sites was difficult to compared between Fig. 2B-b and 2B-c because these peaks were quite weak.

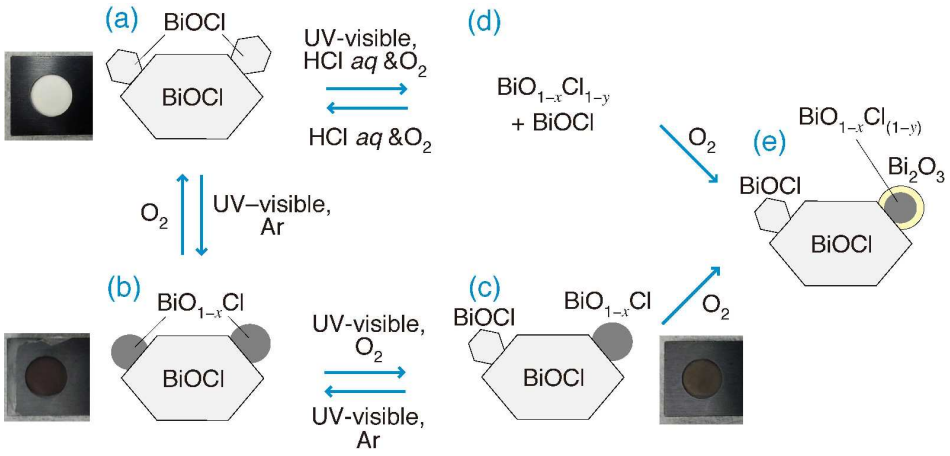

Scheme 3 Proposed structure transformation for BiOCl.

The BiOCl film immersed in HCl aqueous solution (pH 2.0) and during irradiation by UV-visible light at beamline was analyzed using Bi L_3-edge EXAFS (Fig. 3c). The color of the film was light gray. The coordination number of both Bi–O and Bi–Cl decreased (from 4.0 to 2.2 and from 4.0 to 3.1, respectively; Table 1c and Fig. 3c). The oxygen vacancy

should be formed similar to the condition in Ar and UV-visible irradiation. Furthermore, a few percent of chlorine loss/recover was reported for BiOCl immersed in water in response to irradiation/stop of UV light and the transformation was reversible based on the analysis using ion chromatography.[34] The chlorine vacancy based on the decrease of *N*(Bi–Cl) in EXAFS (Table 1c) was in accord with the report.

Then, the UV-visible light was turned off at 60 min of irradiation. Bi L_3-edge EXAFS spectrum was measured at 12 min under dark (Fig. 3d). The EXAFS oscillation was similar to that for sample irradiated by UV-visible light (Fig. 3c1), but the reduced amplitude irradiated by light seems recovered to the level for as-synthesized sample (Fig. 3a1). In fact, the *N*(Bi–O) and *N*(Bi–Cl) values recovered to 4.2 and 4.6 (Table 1d), respectively, similar to that for as-synthesized BiOCl (4.0; Table 1a). Thus, the O and Cl vacancy formed in HCl aqueous solution irradiated by UV-visible light was suggested to be transformed to original BiOCl crystalline state soon after the light was off.

Finally, the BiOCl film that was subjected to five 1-hour cycles of the PFC test (2.5 h of irradiation) and directly exposed to air was analyzed using Bi L_3-edge EXAFS (Fig. 3e). The *N*(Bi–O) values for the as-synthesized BiOCl (4.0) increased to 5.1, whereas the *N*(Bi–Cl) values decreased from 4.0 to 3.1 (Table 1a, e). The *R* values, on the other hand, were essentially constant at 0.244–0.247 and 0.301–0.307 nm, respectively. Notably, the *N*(Bi–O) value (5.1) was similar to that for Bi_2O_3 (5; Table 1f); however, the interatomic distance was longer by 0.014 nm. In contrast to reversible transformation between $BiO_{1-x}Cl_{1-y}$ and BiOCl by on/off exposure to UV-visible light in HCl solution saturated with O_2, the $BiO_{1-x}Cl_{1-y}$ species was not totally transformed back to original BiOCl by the direct exposure to air.

3.2 Photocurrent Changes and the *i–V* Dependence of the PFC

Static PFC tests. In static PFC cycle tests at pH 3.0, following UV–visible irradiation, the photocurrents of the PFC increased and stabilized within 0.84–3.4 min (Fig. 5A). In five light on/off cycles, the photocurrents converged to 32.7–34.0 μA. Similarly, the photocurrents increased and converged to 4.29–4.40 μA within 1.7–4.1 min at pH 4.0. In contrast, at pH 2.0, the current gradually increased and stabilized within 20 min in the first cycle, but did not fully stabilize in the following cycles. The current nearly converged from 102 to 118 μA in five cycles. Separately, photocurrents converged to 106 μA within 60 min at pH 2.0 when the irradiation was continued for 3 h (Fig. 5A'), suggesting reversible structure/state change for BiOCl photocatalyst when the light was off. Throughout this study, the pH values of electrolyte changed negligibly (within a variation of 0.02) over 5 h.

When the UV–visible light was off, the photocurrents quickly decreased to zero within 0.84–4.1 min at pH 2.0, but decreased more slowly (14–20 min) at pH 3.0, and most slowly (25–26 min) at pH 4.0. This trend suggested limited diffusion at lower proton concentrations. Thus, the nearly converged PFC photocurrent values were plotted as a function of the electrolyte solution proton concentrations (Fig. 5B), and it was found that the values increased proportionally to the square root of the proton concentration.

When sulfuric acid solution (pH 2.0) was used for the electrolyte for the photoanode (TiO_2) instead of HCl solution, the converged photocurrent was 76 μA in fitst cycle, but gradually decreased to 77, 63, 64, and 64 μA in five cycles (Fig. 5A"). When the UV–visible light was off, the photocurrents decreased to zero within 3.0–6.5 min under this condition. This response was significantly slower than the relaxation of currents in HCl solution for the photoanode (0.84–4.1 min; Fig. 5A, pH 2.0).

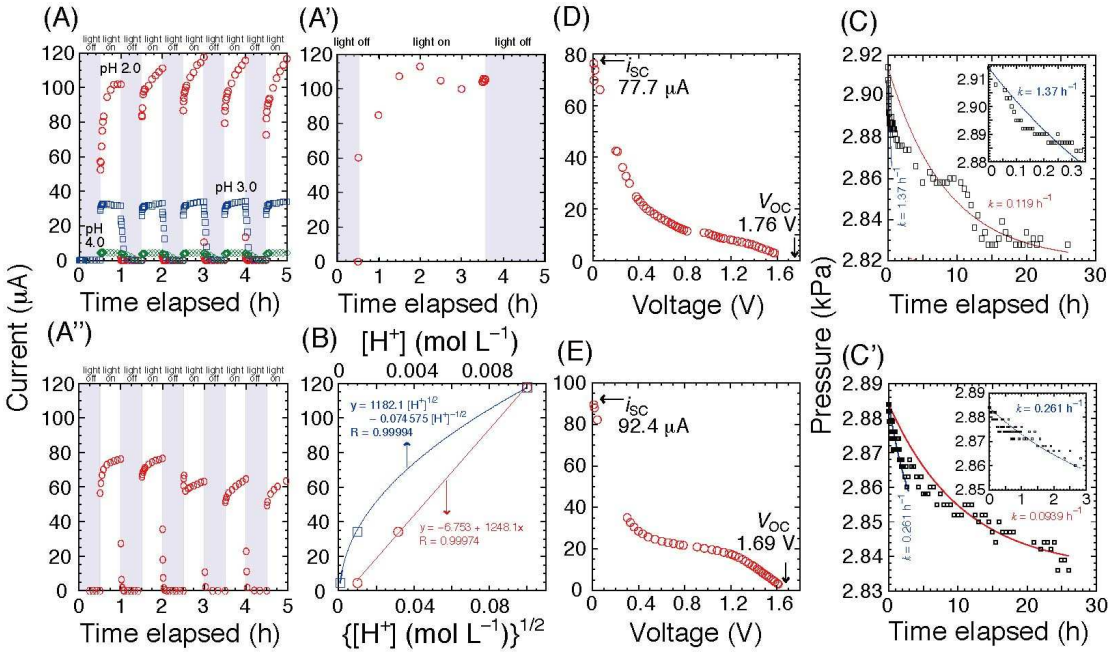

Fig. 5 **(A)** Time course of the photocurrents in the PFC comprised of the TiO_2 and solvo-BiOCl photocatalyst electrodes, which were immersed in HCl solutions at pH of 2.0 (circle, ◦), 3.0 (square, □), and 4.0 (diamond, ◊). **(A')** Continuous test at pH of 2.0 (circle, ◦) was also plotted. **(A")** Time course of the photocurrents in the PFC comprised of the TiO_2 and solvo-BiOCl photocatalyst electrodes, which were immersed in H_2SO_4 and HCl solutions, respectively, both at pH of 2.0 (circle, ◦) **(B)** Correlation between the converged photocurrents within 5 h and the H^+ concentrations of the acidic water in the PFC or the square root of the H^+ concentrations. The fittings were to the linear function (lower *x*-axis) or to the kinetic model equation $i = A[H^+]_c^{1/2} - B[H^+]_c^{-1/2}$ (eq. 7, see text; upper *x*-axis). **(C, C')** Time course of the O_2 pressure in contact with solvo-BiOCl **(C)** and aqua-BiOCl **(C')** previously irradiated with UV–visible light for 12 h. **(D)** *i*–*V* dependence of the PFC comprising TiO_2 and solvo-BiOCl immersed in a pH 2.0 HCl solution. **(E)** *i*–*V* dependence of the PFC comprising TiO_2 and aqua-BiOCl immersed in a pH 2.0 HCl solution.

Reactivity of BiOCl with O_2 gas. For comparison, as-synthesized solvo-BiOCl fine powder was irradiated with UV–visible light for 12 h in vacuum and then in contact with O_2. The quantity of O_2 (2.91 kPa) in a closed glass system corresponded to the dissolved amount of O_2 in acidic water (40 mL) at 290 K. The time course of the reaction for 26 h is shown in Fig. 5C. The rate constant *k* was 0.119 h^{-1} by fitting to the eq. 3. Because the initial reaction

rate was significantly faster than the rate at 26 h, an alternative fitting of the data only for the initial 20 min gave a *k'* value of 1.37 h^{-1} (Fig. 5C, inset).

In the corresponding reactivity test for aqua-BiOCl, the rate constant *k* was 0.093 9 h^{-1} by fitting to the eq. 3 (Fig. 5C'), by 21% smaller compared to that for solvo-BiOCl (Fig. 5C). An alternative fitting of the data for the initial 20 min was difficult for aqua-BiOCl, and the fit of the data for the initial 170 min gave a *k'* value of 0.261 h^{-1} (Fig. 5C', inset).

Furthermore, based on the total O_2 reacted with solvo-BiOCl and aqua-BiOCl irradiated with UV–visible light for 12 h in vacuum (6.1 and 3.6 μmol; Fig. 5C, C'), the stoichiometry of the BiOCl subjected to the kinetic tests of Fig. 5C and C' was estimated to be $BiO_{1-0.023}Cl$ and $BiO_{1-0.014}Cl$, respectively.

***i–V* characteristics.** The *i–V* characteristics were then studied for a PFC comprising TiO_2 and BiOCl at pH 2.0 (Fig. 5D). The *i* value gradually increased as the cell voltage decreased beginning at the open circuit voltage (V_{OC}, 1.76 V), which is similar to the *i–V* dependence for SCs.[62] When the voltage was less than 0.39 V, the current increased linearly from 24.7 to 77.7 μA (short circuit current, i_{SC}), and the maximum electric power (P_{max}) was 10.5 μW (1.01 V × 10.5 μA) for a photocatalyst film area of 1.3 cm^2 (Table 2A).

Table 2 Electrochemical data for PFCs obtained from the *i–V* analysis[a]

	Photocatalyst		V_{OC}	i_{SC}	P_{max}	
Entry	Anode	Cathode	(V)	(μA)	(μW)	Reference
A	TiO_2 (25 nm[b])	solvo-BiOCl (24 nm)	1.76	77.7	10.5	This work
B	TiO_2 (25 nm[b])	aqua-BiOCl (115 nm)	1.69	92.4	21.1	This work
C	TiO_2 (25 nm[b])	Ag(3.0 wt%) –TiO_2 (25 nm[b])	1.59	73.7	14.0	7

[a] The pH of each HCl solution was 2.0. The area of each photocatalyst was 1.3 cm^2

[b] Mean particle size estimated from the XRD pattern; anatase: 21 nm, rutile: 35 nm, anatase/rutile ratio = 7:3

For comparison, the *i*–*V* characteristics of a PFC comprising TiO_2 and aqua-BiOCl at pH 2.0 were also investigated (Fig. 5E). The major difference between the solvo-BiOCl and aqua-BiOCl is the mean particle size: 24 versus 115 nm, respectively, based on the XRD analysis (Fig. 1D, F). Although the V_{OC} value (1.69 V) for the PFC based on the aqua-BiOCl was 0.07 V less than that for the PFC containing the solvo-BiOCl, the former i_{SC} value increased to 92.4 μA, which is 14.7 μA greater than the latter. Consequently, the maximum electric power was 21.1 μW (1.15 V × 18.3 μA) for a photocatalyst film area of 1.3 cm^2 (Table 2B).

3.3 CV for BiOCl

Under N_2 atmosphere. The CV results for BiOCl in a pH 4.0 aqueous HCl solution under N_2 are depicted in Fig. 6A. In the dark, a pair of oxidation and reduction peaks appeared centered at 0.57 and −0.39 V, respectively, versus a standard hydrogen electrode (SHE). The center of the two peaks (0.09 V) coincided with the equilibrium voltage at the pH (Table 3B) for the reaction:

$$BiOCl + 2H^+ + 3e^- \rightarrow Bi + Cl^- + H_2O \qquad (4)$$

Under light irradiation, another pair of oxidation and reduction peaks appeared at 0.75 and −0.19 V, respectively, as shoulder peaks on the redox peaks due to eq. 4 (Fig. 6a). The peak at −0.19 V was very weak. The center of the new peaks (0.28 V) corresponded to the equilibrium voltage (0.32 V @pH 0; Table 3A) for the reaction of the anodic dissolution of Bi and reduction back to Bi:

$$Bi^{3+} + 3e^- \rightarrow Bi \qquad (5)$$

Table 3. Electrochemical data for BiOCl

Redox reaction Conditions	CV peak (V) versus SHE: Reduction wave	Oxidation wave	Center	Equil. voltage @298 K
(A) $Bi^{3+} + 3e^- = Bi$				
O_2, Light	—	—	—	0.3172 @pH 0
O_2, Dark	—	—	—	
N_2, Light	−0.19	0.75	0.28	
N_2, Dark	—	—	—	
(B) $BiOCl + 2H^+ + 3e^- = Bi + Cl^- + H_2O$				
O_2, Light	—	—	—	0.1697−0.0197pH (0.0909 @pH 4.0)
O_2, Dark	−0.39	—	—	
N_2, Light	−0.39	0.57	0.09	
N_2, Dark	−0.39	0.57	0.09	
(C) $Bi_2O_3 + 6H^+ + 6e^- = 2Bi + 3H_2O$				0.376 − 0.0591pH (0.1396 @pH 4.0)
(D) $4H^+ + O_2 + 4e^- = 2H_2O$				1.229 − 0.0591pH (0.993 @pH 4.0)

Under O_2 atmosphere. In the dark, only a weak reduction peak for reaction 4 (−0.39 V) appeared under O_2 (Fig. 6b). Furthermore, no distinct peaks were observed with irradiation of UV–visible light. This contrast suggests a stabilized BiOCl-based phase under an O_2 atmosphere.

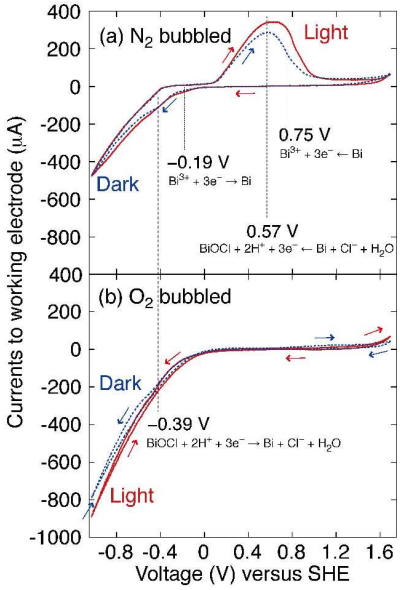

Fig. 6 CV for a BiOCl WE and glassy carbon CE in a pH 4.0 aqueous HCl solution under a (a) N_2 flow and (b) O_2 flow during UV–visible light irradiation (solid lines) or in dark (dotted lines).

4 Discussion

4.1 Phase Transformation of BiOCl

The band gap for as-synthesized BiOCl powder was 3.46 eV (Fig. 1A-a), and the mean disk-like particle size was 24 nm (Fig. 1D). When the BiOCl powder was irradiated with UV–visible light under an Ar atmosphere, the color changed to black in 1 h (Fig. 1A-c and Scheme 3b). The black color turned to gray after 24 h kept under Ar in the dark (Fig. 1A-d) and then back to white when the powder was exposed to air for 5 h (Fig. 1A-e). Thus, (a part of) the crystalline BiOCl changed to something else following UV–visible light irradiation under Ar, but reversibly converted back to BiOCl in air. Furthermore, a new Raman peak appeared at 93 cm^{-1} for BiOCl irradiated by UV-visible light under vacuum due to Bi–Cl stretching vibration (Fig. 1G-b, G'-b). As the peak was not detected for as synthesized BiOCl, new Bi–Cl stretching vibration mode was enabled by the modulation of symmetry for O-deficient BiOCl.

The generation of O defects in the BiOCl irradiated with UV light was suggested on the basis of additional Bi $4f_{5/2}$ and $4f_{7/2}$ peaks at lower binding energy than main peaks due to Bi^{3+} (Fig. 2b). The additional peaks were also reported in literature.[35,60,63] This interpretation was supported by the *N*(Bi–O) decrease (4.0 to 1.9) based on Bi L_3-edge EXAFS analysis for BiOCl irradiated with UV–visible light under Ar (Table 1b and Fig. 3b).

The origin of black color and O deficiency of the BiOCl irradiated with UV–visible light under an Ar atmosphere (Scheme 3b, photograph) was clarified via HR-TEM analysis. A reversible phase transformation from crystalline BiOCl to amorphous-like spherical nanoparticles was observed during the HR-TEM analysis (Fig. 4b3–b6 and the video

available as an *Electronic Supplementary Material*). In contrast, the amorphous-like spherical nanoparticles were rarely observed for the as-synthesized BiOCl (Fig. 4a1–3). Thus, it is concluded that the origin of the black color of the irradiated BiOCl is O-deficient $BiO_{1-x}Cl$. An amorphous-like $BiO_{1-x}Cl$ phase present as spherical nanoparticles in the electron flow of the HR-TEM was observed to reversibly transform to crystalline BiOCl with a clear lattice pattern once O atoms were supplied from inside the crystalline BiOCl grains to achieve phase equilibrium (Figs. 4b3–6 and Scheme 3a and b).

In the HR-TEM images of BiOCl irradiated by UV light under Ar, an outer, ~1 nm-thick layer of the crystalline BiOCl was disordered and considered to be amorphous-like $BiO_{1-x}Cl$.[35,58] Density functional theory (DFT) calculations reported for O displacement in BiOCl from a position in the lattice and generation of vacancies in the BiO^+ layers revealed the formation of an additional energy state slightly below the CB of BiOCl. Such vacancies would function as electron trapping sites; however, they could also recombine with the displaced O under equilibrium conditions.[64]

The electron currents at the position of the sample in the JEM-2100F were 500 pA cm^{-2} at maximum. Thus, considering the elementary charge, 4×10^9 electrons per second reached the 1.3 cm^2 of sample. In comparison, the photon flux from the SX-UID502XAM via the fiber light guide was 2×10^{16} photons s^{-1}, and generated photocurrents for the PFC were 7×10^{14} electrons s^{-1} (118 μA at most; Fig. 5A) to the photocatalyst film area of 1.3 cm^2 (Scheme 1). Although the physical situation for the electron flow to BiOCl in the HR-TEM versus the charge separation for TiO_2 and BiOCl following irradiation and the resulting PFC current is different, the effective electron flow during the PFC tests was approximately 10^5 times greater than that in the HR-TEM apparatus.

In the XP spectra in Bi $4f_{5/2}$ and Bi $4f_{7/2}$ regions, weaker peaks were detected at 162.2 and 157.0 eV on the lower energy side of major peaks at 164.8(±0.1) and 159.5(±0.1) eV,

respectively, for BiOCl irradiated by UV-visible light in Ar or in HCl aqueous solution saturated with O_2 (Fig. 2b, c). The weaker peaks suggested reduced Bi state at the valence between 3 and 0, shifted by 2.5–2.6 eV toward lower energy side from major peaks due to Bi^{3+} state. Furthermore, both O and Cl-deficient structure was directly confirmed by the decrease of *N*(Bi–O) and *N*(Bi–Cl) values from 4 to 2.2 and 4 to 3.1, respectively (Fig. 3c and Table 1c), based on Bi L_3-edge EXAFS in HCl aqueous solution (pH 2.0) saturated with O_2 irradiated by UV-visible light. Thus, $BiO_{1-x}Cl$ formed in Ar (Scheme 3b) further lost a part of chlorine ($BiO_{1-x}Cl_{1-y}$), but it transformed back to BiOCl when the light was off (Fig. 3d, Table 1d, and Scheme 3a) in accordance with literature.[34] In relation to the EXAFS results, reduction peak due to Cl loss via eq. 4 was observed at −0.39 V in HCl aqueous solution with N_2 or O_2 (Fig. 6a, b).

In summary, amorphous-like $BiO_{1-x}Cl$ spherical nanoparticles (Scheme 3b) would be present in the BiOCl samples irradiated with UV–visible light under Ar and for which the UV–visible spectra (Fig. 1A-b–d), XRD patterns (Fig. 1E), Bi $4f_{5/2}$ and $4f_{7/2}$ XPS peaks (Fig. 2b), and Bi L_3-edge EXAFS measurements (Fig. 3b) were obtained. Both O and Cl-deficient $BiO_{1-x}Cl_{1-y}$ species should be present for the BiOCl film on the photocathode irradiated by UV-visible light immersed in HCl solution under O_2 gas for XPS (Fig. 2c), Bi L_3-edge EXAFS (Fig. 3c), and during the PFC tests (Fig. 5A).

It is thought that the O and/or Cl-deficient $BiO_{1-x}Cl_{1-y}$ or $BiO_{1-x}Cl$ nanoparticles were covered with thin Bi_2O_3 layers (Scheme 3e) in samples subjected to UV–visible (Fig. 1C) and EXAFS (Fig. 3e) analyses and used in the PFC tests in HCl with light irradiation and directly exposed to air.

4.2 Factors for Controlling PFC Performance

The V_{OC}, i_{SC}, and P_{max} values were summarized in Table 2 based on the *i*–*V* characteristics. Although the theoretical maximum electromotive force for the PFC comprising TiO_2 and BiOCl is 2.75 V in the energetic diagram (Scheme 1), the best V_{OC} value obtained in this study was 1.69–1.76 V (Fig. 5D, E). It is also possible that the carrier level of the ITO [work function (WF) 4.6–4.8 eV] determined the voltage of the photoexcited electrons to the CB of TiO_2 (WF 4.13–4.3 eV)[65,66] if the ITO film behaved like a semiconductor rather than a conductor. If this logic applies, the voltage loss due to the difference in the WF is 0.3–0.67 V, and the theoretical maximum voltage of 2.75 V would be reduced to 2.08–2.45 V.

Even so, the V_{OC} values (1.69–1.76 V) were still higher for the PFC comprising TiO_2 and solvo/aqua-BiOCl than the 1.59 V reported for the PFC comprising TiO_2 and Ag–TiO_2 (Table 2).[7] Depending on the energy diagram (Scheme 1), the maximum electromotive force is theoretically smaller for the PFC comprising TiO_2 and BiOCl (2.75 V) than that for the PFC comprising TiO_2 and Ag–TiO_2 (3.0 V).[7] In this context, the combination of n- and p-semiconductors was advantageous for minimizing the overpotential compared to rectification by the Schottky barrier.

4.3 Kinetics of the PFC

Derivation of kinetics. The photocurrents in the present PFCs are generated by the balance between the photoexcitation and charge recombination both in the TiO_2 and BiOCl photocatalysts, and the reaction rates of water photooxidation and O_2 photoreduction (Scheme 1). The allowed indirect[53,67] and direct[58] (Fig. 1B) band gap electronic transitions lead to the separation of electrons and holes in TiO_2 and BiOCl, respectively, and equilibrium

constants for charge separation (K_a and K_c) are assumed in the anodic TiO_2 and cathodic BiOCl, respectively.

The photooxidation over TiO_2 was essentially irreversible under a N_2 flow, which purged the generated O_2. The superiority of HCl aqueous solution (pH 2.0) to H_2SO_4 aqueous solution (pH 2.0) as an electrolyte for the photoanode was demonstrated (Fig. 5A and A"). One of the major reasons would be the difference of molar conductivity of the solutions (411.1 versus 336.4 S cm^2 mol^{-1}).[68] The converged photocurrents gradually increased in Fig. 5A using HCl solution in contrast to decrease in Fig. 5A" using H_2SO_4 solution. This difference suggested the inhibition of hole transfer from surface to water molecule due to the blocking of Ti sites by sulfate ions. Greater blocking effects of Ti sites by the anions of electrolyte were reported for the photodecomposition 2-chloro-2′,6′-diethyl-*N*-(methoxymethyl)acetanilide and the order of the effects was in the order

$$PO_4^{3-} > NO_3^- > SO_4^{2-} > Cl^-.^{69} \qquad (6)$$

The rate and rate constant for this reaction are denoted as r_{ox} and k_{ox}, respectively. The O_2 photoreduction at BiOCl was in equilibrium with the product (water), and the constant is denoted as K_{red}. Based on the principles of PFCs, the forward electron flow rate from TiO_2 to BiOCl via the external circuit should be proportional to both the excited electron concentration in TiO_2 and the hole concentration in BiOCl (Scheme 1). In addition, the reverse electron flow rate should be proportional to both the unreacted excited electron concentration at BiOCl and the unreacted hole concentration at TiO_2. Thus, the effective electron flow rate (photocurrent i) is formulated in eq. 7. The derivation is shown in eqs. S1–S4 (ESI†).

$$i = k\frac{K_a'(k_{ox}')^{\frac{1}{4}}(K_c')^{\frac{1}{6}}(K_{red}')^{\frac{1}{8}}}{(r_{ox})^{\frac{1}{4}}}([O_2]_c)^{\frac{1}{8}}\left(\left[H^+\right]_c\right)^{\frac{1}{2}} - k'\frac{(r_{ox})^{\frac{1}{4}}(K_c')^{\frac{1}{6}}}{(k_{ox}')^{\frac{1}{4}}(K_{red}')^{\frac{1}{8}}}\frac{1}{([O_2]_c)^{\frac{1}{8}}\left(\left[H^+\right]_c\right)^{\frac{1}{2}}}, \qquad (7)$$

where [O_2] and [H^+] with a subscript "c" denote the concentrations of O_2 and H^+ in the acidic solution around the cathode, and the rate and equilibrium constants with the prime symbol denote the constants multiplied with essentially constant concentrations for the predominant species in the acidic solution/photocatalysts (see ESI† for a detailed definition).

Comparison of kinetics to experimental data. Fitting of the experimental data for the pH dependence in eq. 7 is presented in Fig. 5B, upper *x*-axis. The second term was negligible in the fitting to eq. 7 ($i = 1182\ [H^+]^{1/2} - 0.07458\ [H^+]^{-1/2}$), demonstrating that the reverse electron flow from the CB of BiOCl to the VB of anodic TiO_2 via the external circuit was minimal. Moreover, the net photocurrents were in fact proportional to $[H^+]^{1/2}$ (Fig. 5B, lower *x*-axis) in accordance with eq. 7.

A kinetic equation similar to eq. 6 was reported for the PFC comprising TiO_2 and Ag–TiO_2.[7] The fitted equation for the pH dependence was $i = 626.7\ [H^+]^{1/2} - 0.009977\ [H^+]^{-1/2}$. The coefficient of the second term was even smaller than that for the p–n type PFC of the present study because of the rectification by the Schottky barrier between the TiO_2 and Ag nanoparticles. Notably, the combination of TiO_2 and BiOCl was nearly a factor less efficient with respect to rectification.

Conversely, the coefficient of the first term was greater for the p–n type PFC compared to that for the Schottky-type PFC (1182 *versus* 626.7, respectively). Faster charge transfer rates (holes to H_2O at the anode and electrons to O_2 at the cathode) at the interfaces between the photocatalysts and the acidic solution due to band bending[14,15] should enhance the first term: the i_{SC} values of 77.7–92.4 μA (Table 2A and B) versus 73.7 μA for the Schottky-type PFC[7] (Table 2C).

Another reason for this difference is the layered structure of BiOCl. If a Cl 3p electron is excited to Bi 6p (Figs. 1A and C) upon irradiation with UV–visible light, the holes and electrons should preferably diffuse in the Cl^- and BiO^+ layers, respectively, both of which are

in the 001 plane.[13] The crystallines of solvo-BiOCl tended to grow in the perpendicular direction to [001] whereas the crystallines of aqua-BiOCl tended to grow in the direction of [001] (Fig. 1D, F). Therefore, charges separated in bulk would effectively diffuse in the 001 plane and favorably reach photocatalyst surface, e.g. {100} and {110}, for aqua-BiOCl,[13] in accord with the PFC performances (Table 1A, B). Alternatively, aqua-BiOCl was advantageous to solvo-BiOCl because the greater crystallines led to smaller serial resistance[70] of cathode photocatalyst film.

Red-ox of Bi sites. The peaks for the reduction of BiOCl to Bi^0 and the reverse oxidation reaction (eq. 4) were observed in a pH 4.0 acidic solution under N_2 (Fig. 6a and Table 3B). When the electrode was irradiated with UV–visible light, weaker peaks for the reduction of Bi^{3+} to Bi^0 and the reverse oxidation reaction (eq. 5) were also detected (Table 3A). In contrast, in a pH 4.0 acidic solution under O_2 in the dark, only a very weak peak for the reduction of BiOCl to Bi^0 was observed, and during irradiation, no CV peaks appeared (Fig. 6b).

The Bi^0 species formed at voltages lower than −0.19 V during the CV experiments was not detected via XRD, XPS, EXAFS, or HR-TEM analysis of BiOCl irradiated under Ar or O_2. The color change from white to black (under Ar) or gray (under air/O_2) was due to O-deficient $BiO_{1-x}Cl$ species formed because of UV–visible light irradiation. Under vacuum and irradiation of UV-visible light for 12 h, the stoichiometry of sample was estimated to $BiO_{1-0.023}Cl$ for solvo-BiOCl and $BiO_{1-0.014}Cl$ for aqua-BiOCl based on kinetic study with O_2 gas (Fig. 5C, C'). Amorphous-like $BiO_{1-x}Cl$ particles (~5 nm) were observed in the HR-TEM image (Fig. 4b3, 5, 6, 7), and these particles reversibly transformed to crystalline BiOCl (Fig. 4b4, 5) because of the balance of electron flows in the HR-TEM apparatus and the O supply from the supporting BiOCl grains.

The presence of $BiO_{1-x}Cl_{1-y}$ species in HCl aqueous solution (pH 2.0) and O_2 gas irradiated by UV-visible light was proposed by weaker peaks at 162.2 and 157.0 eV at lower binding energy side for $4f_{5/2}$ and $4f_{7/2}$ for Bi^{3+} state of BiOCl crystallines in XPS (Fig. 2c) and reduced *N*(Bi–O) and *N*(Bi–Cl) values (Table 1c) given by Bi L_3-edge EXAFS (Fig. 3c). No peaks corresponding to Bi^0 and no metallic Bi–Bi bonds were detected in XPS and EXAFS, respectively.

Reaction steps. The converged photocurrent (118 μA, Fig. 5A) of the PFC at pH 2.0 corresponds to 1.8 mmol-e^- h^{-1} $g_{BiOCl}{}^{-1}$, which is ten times as fast as the reaction rate of the black solvo-$BiO_{1-x}Cl$ with O_2: $k \times 0.206$ mmol (initial O_2 amount)/0.135 g_{BiOCl} = 0.18 mmol-O_2 h^{-1} $g_{BiOCl}{}^{-1}$ based on the fitting for 26 h, but on the same order as the initial reaction rate *k*' during the first 20 min (2.1 mmol-O_2 h^{-1} $g_{BiOCl}{}^{-1}$). The initial higher rate suggests that the reaction with O_2 first occurs at surface $BiO_{1-x}Cl$ sites (or $BiO_{1-x}Cl_{1-y}$ in HCl aqueous solution), rather than at bulk sites. The *k* value for 26 h was almost reproduced for solvo- and aqua-BiOCl (1.37 versus 0.0939 h^{-1}; Fig. 5C, C'), but the initial fast reaction at surface $BiO_{1-x}Cl$ sites was difficult to follow for aqua-BiOCl due the lower dispersion (greater mean particle size (see section 3.1.1, Fig. 1D, F).

On the basis of these results, a mechanism for photocatalysis by BiOCl has been proposed. In the PFC, a part of BiOCl on the photocathode immersed in HCl at a pH of 2.0–4.0 is thought to be photoreduced to $BiO_{1-x}Cl_{1-y}$ (Scheme 3d) in a manner similar to that described in eq. 4:

$$BiOCl\ (surface) + 2xH^+ + (2x+y)e^- \rightarrow BiO_{1-x}Cl_{1-y}\ (surface) + yCl^- + xH_2O \qquad (8)$$

Reaction 4 was observed as a CV peak at −0.39 V in O_2 atmosphere, but only in the dark (Fig. 6b). The reaction with O_2 at the $BiO_{1-x}Cl_{1-y}$ surface sites irradiated by UV-visible light (2.1 mmol-O_2 h^{-1} $g_{cat}{}^{-1}$, C) follows eq. 9:

$$2BiO_{1-x}Cl_{1-y}\ (surface) + xO_2 \rightarrow 2BiOCl_{1-y}\ (surface) \qquad (9)$$

Summing up eqs. 8 and 9, eq. 10 is obtained:

$$4H^+ + O_2 + 4e^- \rightarrow 2H_2O \qquad (10)$$

in which the partial dissolution of Cl was neglected because it was not related to photoconversion of H_2O and O_2. The total current generated in Fig. 5A (pH 2.0) corresponded to 9.7 μmol-e^-, whereas the quantity of the BiOCl mounted on the cathode was 9.6 μmol. Because the oxygen vacancy (x) in $BiO_{1-x}Cl$ irradiated by UV-visible light was estimated to 2.3% (Fig. 5C), the cathode reaction should be catalytic.

Suggested active species for the catalysis using BiOCl-based photocatalysts were summarized in Table 4. Due to the exposure to UV and/or visible light, black/gray $BiO_{1-x}Cl$ was suggested to be active species for dyes and 2-naphthol degradation.[35,58,60] The Cl dissolution via the reaction of ·Cl and electron was also reported to form $BiOCl_{1-x}(OH)_x$.[34] On the other hand, metallic Bi nanoparticles were suggested on BiOCl or $BiO_{1-x}Cl$ surface using reducing agent, e.g. oxalate and ethanol effective for dyes, acetophenone, and *p*-chlorobenzaldehyde degradation.[10,63] Furthermore, the reactivity of O-defect to form $\cdot O_2^-$ and O_2^{2-} was proposed over (001) and (010) surface of $BiO_{1-x}Cl$, respectively, for the O_2 reduction based on DFT calculations.[71]

In this study, in-situ spectroscopic monitoring of BiOCl during photocatalysis was performed for the first time by Bi L_3-edge EXAFS (Fig. 3c). No special reducing agent[10,63] was used in this study. Thus, active species $BiO_{1-x}Cl_{1-y}$ (Scheme 3d) proposed based on XPS (Fig. 2c), EXAFS (Fig. 3c), and reactivity test with O_2 (Fig. 5C) is in consistent with the suggested active structure in refs. 34, 35, 60, and 58 and reaction route via eq. 9 is in consistent with ref. 71.

In addition to plausible incorporation as active sites in eq. 9, the O-deficient state of $BiO_{1-x}Cl_{(1-y)}$ is slightly lower than that of the CB of BiOCl. Consequently, it can effectively trap photoexcited electrons[59,73] and contribute to the photocatalysis via transfer of the trapped electrons to O_2 molecules in a similar manner to that observed for dye photodecomposition in the presence of O_2[35,58,73] and as predicted by DFT calculations for the (001) surface.[71]

Table 4. Suggested active species using BiOCl and the derivatives as photocatalysts

Substrate	Medium	Type of light	Catalyst	Suggested Active species	Ref.
Rhodamine B	Water & air	UV (254 nm)	(001)-preferered BiOCl	BiOCl	60
Rhodamine B	Water & air	Vis (>420 nm)	(001)-preferered BiOCl	BiOCl	60
Methyl orange	Dil. HCl aq & N_2	High *P* Hg	BiOCl	$BiOCl_{1-x}(OH)_x$	34
Methyl orange	Dil. HCl aq & air	High *P* Hg	BiOCl	$BiOCl_{1-x}(OH)_x$	34
Phenol	Water & air	High *P* Hg	BiOCl	$BiOCl_{1-x}(OH)_x$	34
Rhodamine B	Water & air	High *P* Xe (>400 nm)	BiOCl under UV in Ar	$BiO_{1-x}Cl$	35
2-naphthol degrad.	Water & air	Vis	(010)-preferred BiOCl	$BiO_{1-x}Cl$	60
Methene blue	Water & air	W–halogen (>420 nm)	UV-reduced BiOCl	$BiO_{1-x}Cl$	58
Methyl orange	Water & air	Wideband	$C_2O_4^{2-}$-reduced BiOCl	Bi^0-BiOCl	10
Rhodamine B	Water & air	Vis	EtOH/HCl-reduced BiOCl	Bi^0-$BiO_{1-x}Cl$	63
Methyl blue	Water & air	Vis	EtOH/HCl-reduced BiOCl	Bi^0-$BiO_{1-x}Cl$	63
Eosin B	Water & air	Vis	EtOH/HCl-reduced BiOCl	Bi^0-$BiO_{1-x}Cl$	63
Coomassie brilliant blue	Water & air	Vis	EtOH/HCl-reduced BiOCl	Bi^0-$BiO_{1-x}Cl$	63
Acetophenone	Water & air	Vis	EtOH/HCl-reduced BiOCl	Bi^0-$BiO_{1-x}Cl$	63
p-chlorobenzaldehyde	Water & air	Vis	EtOH/HCl-reduced BiOCl	Bi^0-$BiO_{1-x}Cl$	63
Rhodamine B	Water & air	UV (365 nm)	Ultrathin BiOCl	Bi-defect	72
Rhodamine B	Water & air	Xe (>420 nm)	Ultrathin BiOCl	Bi-defect	72
O_2 reduction	—	(DFT)	(001) face	O-defect to form $\cdot O_2^-$	71
O_2 reduction	—	(DFT)	(010) face	O-defect to form O_2^{2-}	71

4.4 Energetic Efficiency of the PFC

The quantum efficiency of the PFC was evaluated on the basis of the absorption (6.9%) by the photocatalyst of the incident light (1.7×10^{17} photons s^{-1}) that the photocatalyst layers were exposed to and the short circuit current (92.4 μA ~ 5.7×10^{14} electrons s^{-1}; Fig. 5E). The overall efficiency of the cell current per absorbed light was 0.024 and is considered as the product of the efficiencies of the anode (TiO_2) and the cathode (BiOCl). If a similar

efficiency is assumed for electron generation at the CB of the anode and hole generation at the VB of the cathode, then the efficiencies of the anode and cathode were each approximately 0.16 (0.16 × 0.16 = ~0.024). Practically, as the absorbance at the photocatalyst film was low (6.9%), true overall efficiency was lower (0.0017), that may be divided into the contribution of anode and cathode: 0.041 × 0.041 = 0.0017.

Next, the contribution of the entropy of mixing (ΔS_{mix}) was considered for an equivalent amount of N_2 and O_2 supplied to the photoanode and photocathode, respectively, in comparison to the concentration cells.[74] When the maximum power was produced by the PFCs comprising TiO_2 and solvo-BiOCl (Fig. 5D) or aqua-BiOCl at pH 2.0 (Fig. 5E), the power generation efficiencies were 10.5 μW (1.01 V × 10.5 μA) and 21.1 μW (1.15 V × 18.3 μA), respectively, versus the energy generated because of mixing of N_2 and O_2 ($T\Delta S_{mix}$) per second:

$$T\Delta S_{\text{mix}} = -RT(n_{\text{N}_2}\ln x_{\text{N}_2} + n_{\text{O}_2}\ln x_{\text{O}_2}) = -8.31\times 290\times 2\times \frac{10.5\times 10^{-6}}{4\times 9.65\times 10^{4}}\ln\frac{1}{2} = 0.091\mu\text{W}, \quad (11)$$

and

$$T\Delta S_{\text{mix}} = -8.31\times 290\times 2\times \frac{18.3\times 10^{-6}}{4\times 9.65\times 10^{4}}\ln\frac{1}{2} = 0.16\mu\text{W}, \quad (12)$$

respectively. Thus, the contribution of the entropy of mixing of the feed gases was negligible, and the light energy for band gap excitation at both the anode and cathode exclusively generated power up to 21.1 μW (Table 2B). The electromotive force of the PFC can thus be explained on the basis of the energy diagram in Scheme 1, including the equilibrium charge separation at the anode and cathode following irradiation, rather than the simple difference in the concentrations of O_2 and the Gibbs free energies for the O_2 fractions at the anode and cathode for the concentration cells.[74]

5 Conclusions

A PFC comprising two photocatalysts (TiO_2 and BiOCl) was demonstrated to achieve V_{OC} values of 1.69–1.76 V on the basis of the difference in the CB minimum of TiO_2 and the VB maximum of BiOCl, which are greater than those for PECs, dye-sensitized SCs, and a PFC comprising TiO_2 and Ag–TiO_2.[7] The greater particle size (mean 115 nm) of aqua-BiOCl was advantageous by facilitating electron transfer from particle to particle, whereas the smaller particle size (mean 24 nm) of solvo-BiOCl was advantageous for suppressing charge recombination within the nanoparticles. The maximum power was 21.1 μW for the PFC comprising TiO_2 and aqua-BiOCl, and the energetic efficiency per absorbed light at photocatalysts was estimated as the product (0.024) of electron generation at TiO_2 (0.16) and hole generation at BiOCl (0.16) for recombination via the external circuit.

A portion of the BiOCl nanoparticles was transformed into amorphous-like $BiO_{1-x}Cl$ nanoparticles because of irradiation with UV–visible light and then reversibly transformed back in a vacuum (HR-TEM and Raman) or under Ar (UV–visible spectroscopy and XPS) when the light was turned off. These O-deficient nanoparticles were the origin of black color of the irradiated BiOCl. In addition, a BiOCl sample sufficiently irradiated with UV–visible light reacted with the quantity of O_2 gas corresponding to the dissolved amount in the HCl solution in the PFC at a rate (2.1 mmol-O_2 h^{-1} $g_{BiOCl}{}^{-1}$) during the initial 20 min that was on the same order as the photocurrent of the PFC (1.8 mmol-e^- h^{-1} $g_{BiOCl}{}^{-1}$), suggesting that surface O-deficient $BiO_{1-x}Cl$ sites may contribute to the photocatalytic O_2 reduction in the PFC. The reduced Bi sites observed for BiOCl in Ar irradiated by UV-visible light was also detected but further lost a part of Cl as $BiO_{1-x}Cl_{1-y}$ in HCl aqueous solution (pH 2.0) in O_2 irradiated by UV-visible light by Bi 4f XPS and Bi L_3-edge EXAFS. Again, the reaction of O-deficient $BiO_{1-x}Cl_{1-y}$ sites with O_2 and subsequent reaction with protons and electrons suggested catalytic cycle for O_2 reduction in the PFC.

† Electronic supplementary information (ESI) available: The derivation of eq. 6 for PFC photocurrents. See http://www.rsc.org/suppdata/ta/c4/******.

Acknowledgments

The authors are grateful for financial support from the Feasibility Study Stage of A-STEP (AS251Z00906L, AS231Z01459C) from the Japan Science and Technology Agency, the Iwatani Naoji Foundation (2011–2012), and a Grant-in-Aid for Scientific Research C (26410204, 22550117) from Japan Society for the Promotion of Science. X-ray absorption experiments were conducted under the approval of the Photon Factory Proposal Review Committee (2013G159). We appreciate Dr. Takeo Soejima at JASCO for Raman measurements and Yoshihide Yoshida and Tohru Maki at the Analytical & Measuring Instruments Division, Shimadzu Corporation for XPS measurements.

References

1 N. S. Lewis and D. G. Nocera, *Proc. Natl. Acad. Sci. U. S. A.,* 2006, **103**, 15729–15735.

2 Y. Izumi, *Coord. Chem. Rev.*, 2013, **257**, 171–186.

3 J. R. Bolton, *Sol. Energy*, 1996, **57**, 37–50.

4 M. Grätzel, *Nature*, 2001, **414**, 338–344.

5 H. A. Gasteiger and N. M. Marković, *Science*, 2009, **324**, 48–49.

6 K. S., Joya, Y. F. Joya, K. Ocakoglu, and R. van de Krol, *Angew. Chem. Int. Ed.*, 2013, **52**, 10426–10437.

7 Y. Ogura, S. Okamoto, T. Itoi, Y. Fujishima, Y. Yoshida, and Y. Izumi, *Chem. Comm.*, 2014, **50**, 3067–3070.

8 H. Cheng, B. Huang, and Y. Dai, *Nanoscale*, 2014, **6**, 2009–2026.

9 Y. Bessekhouad, D. Robert, and J. V. Weber, *Catal. Today*, 2005, **101**, 315–321.

10 S. Weng, B. Chen, L. Xie, Z. Zheng, and P. Liu, *J. Mater. Chem. A*, 2013, **1**, 3068–3075.

11 X. Chen and S. S. Mao, *Chem. Rev.*, 2007, **107**, 2891–2959.

12 N. Serpone, *J. Phys. Chem. B*, 2006, **110**, 24287–24293.

13 K. L. Zhang, C. M. Liu, F. Q. Huang, C. Zheng, and W. D. Wang, *Appl. Catal. B*, 2006, **68**, 125–129.

14 M. S. Wrighton, *Acc. Chem. Resear.*, 1979, **9**, 303–310.

15 M. S. Wrighton, A. B. Ellis, P. T. Wolczanski, D. L. Morse, H. B. Abrabamson, D. S. Ginley, *J. Am. Chem. Soc.*, 1976, **98**, 2774–2779.

16 Z. Li, L. Yu, Y. Liu, and S. Sun, *Electrochim. Acta*, 2014, **129**, 379–388.

17 G. W. Ho, K. J. Chua, and D. R. Siow, *Chem. Engineer. J.*, 2012, **181/182**, 661–666.

18 K. Li, Y. Xu, Y. He, C. Yang, Y. Wang, and J. Jia, *Environ. Sci. Technol.*, 2013, **47,** 3490–3497.

19 P. Lianos, *J. Hazard. Mater.*, 2011, **185**, 575–590.

20 B. D. Alexander, P. J. Kulesza, I. Rutkowska, R. Solarska, and J. Augustynski, *J. Mater. Chem.*, 2008, **18**, 2298–2303.

21 K. Ren, K.; Y. X. Gan, T. J. Young, Z. M. Moutassem, and L. Zhang, *Composites: B*, 2013, **52**, 292–302.

22 K. Ren, C. A. McConnell, Y. X. Gan, A. A. Afjeh, and L. Zhang, *Electrochim. Acta*, 2013, **109**, 162–167.

23 J. Yang, D. Wang, and C. Li, *Accounts Chem. Resear.*, 2013, **46**, 1900–1909.

24 C. Leygraf, M. Hendewerk, and G. A. Somorjai, *J. Phys. Chem.*, 1982, **86**, 4484–4485.

25 A. Berger, R. A. Segalman, and J. Newman, *Energy Environ. Sci.*, 2014, **7**, 1468–1476.

26 Z. Wang, R. R. Roberts, G. F. Naterer, and K. S. Gabriel, *Internat. J. Hydrogen Energy*, 2012, **37**, 16287–16301.

27 R. C. Kainthla, B. Zelenay, and J. O'M. Bockris, *J. Electrochem. Soc.*, 1987, **134**, 841–845.

28 K. Sayama, K. Mukasa, R. Abe, Y. Abe, and H. Arakawa, *Chem. Commun.*, 2001, **35**, 2416–2417.

29 K. Fujihara, T. Ohno, and M. Matsumura, *J. Chem. Soc. Faraday Trans.*, 1998, **94**, 3705–3709.

30 M. C. Hanna and A. J. Nozik, *J. Appl. Phys.*, 2006, **100**, 074510.

31 M. Morikawa, Y. Ogura, N. Ahmed, S. Kawamura, G. Mikami, S. Okamoto, and Y. Izumi, *Catal. Sci. Technol.*, 2014, **4**, 1644–1651.

32 A. Heller, *Acc. Chem. Resear.*, 1981, **14**, 154–162.

33 Q. Chen, J. Li, X. Li, K. Huang, B. Zhou, W. Cai, and W. Shangguan, *Environ. Sci. Technol.*, 2012, **46**, 11451–11458.

34 F. Chen, H. Liu, S. Bagwasi, X. Shen, and J. Zhang, *J. Photochem. Photobio. A*, 2010, **215**, 76–80.

35 L. Ye, K. Deng, F. Xu, L. Tian, T. Peng, and L. Zan, *Phys. Chem. Chem. Phys.*, 2012, **14**, 82–85.

36 N. Ahmed, Y. Shibata, T. Taniguchi, and Y. Izumi, *J. Catal.*, 2011, **279**, 123–135.

37 N. Ahmed, M. Morikawa, and Y. Izumi, *Catal. Today*, 2012, **185**, 263–269.

38 F. Wooten, *Optical Properties of Solids*, Academic Press, New York, U. S. A., 1972, p.142.

39 W. L. Huang and Q. Zhu, *Computational Mater. Sci.*, 2008, **43**, 1101–1108.

40 X. Zhang, C. Fan, Y. Wang, Y. Wang, Z. Liang, and P. Han, *Computational Mater. Sci.*, 2013, **71**, 135–145.

41 J. F. Moulder, W. F. Stickle, P. E. Sobol, and K. D. Bomden, *Handbook of X-ray Photoelectron Spectroscopy*, J. Chastain, ed., Perkin-Elmer Co., Minnesota, U. S. A., 1992.

42 K. Oka, Y. Ogura, and Y. Izumi, *J. Power Sources*, 2014, **258C**, 83–88.

43 S. Wada, K. Oka, K. Watanabe, and Y. Izumi, *Frontiers Chem.*, 2013, **1**, Article 8.

44 Y. Izumi, H. Nagamori, F. Kiyotaki, D. Masih, T. Minato, E. Roisin, J.-P. Candy, H. Tanida, and T. Uruga, *Anal. Chem.*, 2005, **77**, 6969–6975.

45 Y. Izumi and H. Nagamori, *Bull. Chem. Soc. Jpn.*, 2000, **73**, 1581–1587.

46 M. Morikawa, N. Ahmed, Y. Yoshida, and Y. Izumi, *Appl. Catal. B*, 2014, **144**, 561–569.

47 Y. Yoshida, Y. Mitani, T. Itoi, and Y. Izumi, *J. Catal.*, 2012, **287**, 190–202.

48 Y. Izumi, K. Konishi, and H. Yoshitake, *Bull. Chem. Soc. Jpn.*, 2008, **81**, 1241–1249.

49 Y. Izumi, K. Konishi, D. Obaid, T. Miyajima, and H. Yoshitake, *Anal. Chem.*, 2007, **79**, 6933–6930.

50 J. A. Bearden, *Rev. Mod. Phys.*, 1967, **29**, 78–124.

51 M. Vaarkamp, H. Linders, and D. Koningsberger, *XDAP version 2.2.7*, XAFS Services International, Woudenberg, The Netherlands, 2006.

52 K. Oka, Y. Shibata, T. Itoi, and Y. Izumi, *J. Phys. Chem. C*, 2010, **114**, 1260–1267.

53 Y. Izumi, T. Itoi, S. Peng, K. Oka, and Y. Shibata, *J. Phys. Chem. C*, 2009, **113**, 6706–6718.

54 L. Ankudinov, B. Ravel, J. J. Rehr, and S. D. Condradson, *Phys. Rev. B*, 1998, **58**, 7565–7576.

55 P. Cucka and C. S. Barrett, *Acta Cryst.*, 1962, **15**, 865–872.

56 N. Jiang and J. C. H. Spence, *J. Phys. Conden. Matter*, 2006, **18**, 8029–8036.

57 S. C. Nyburg, G. A. Ozin, and J. T. Szymański, *Acta Cryst. B*, 1971, **27**, 2298–2304.

58 B. Sarwan, B. Pare, and A. D. Acharya, *Mater. Sci. Semicond. Process.*, 2014, **25**, 89–97.

59 X. Zhang, T. Guo, X. Wang, Y. Wang, C. Fan, and H. Zhang, *Appl. Catal. B*, 2014, **150/151**, 486–495.

60 S. Weng, J. Hu, M. Lu, X. Ye, Z. Pei, M. Huang, L. Xie, S. Lin, and P. Liu, *Appl. Catal. B*, 2015, **163**, 205–213.

61 X. Zhang, X. B. Wang, L. W. Wang, W. K. Wang, L. L. Long, W. W. Li, and H. Q. Yu, *Appl. Mater. Interf.*, 2014, **6**, 7766–7772.

62 A. Y. Anderson, P. R. Barnes, J. R. Durrant, and B. C. O'Regan, *J. Phys. Chem. C*, 2011, **115**, 2439–2447.

63 Y. Yu, C. Cao, H. Liu, P. Li, F. Wei, Y. Jiang, and W. Song, *J. Mater. Chem. A*, 2014, **2**, 1677–1681.

64 X. Zhang, L. Zhao, C. Fan, Z. Liang, P. Han, *Computational Mater. Sci.*, 2012, **61**, 180–184.

65 A. Imanishi, E. Tsuji, and Y. Nakato, *J. Phys. Chem. C*, 2007, **111**, 2128–2132.

66 D. O. Scanlon, C. W. Dunnill, J. Buckeridge, S. A. Shevlin, A. J. Lodsdail, S. M. Woodley, R. A. Catlow, M. J. Powell, R. G. Palgrave, I. P. Parkin, G. W. Watson, T. W. Keal, P. Sherwood, A. A. Sokol, *Nature Mater.*, 2013, **12**, 798–801.

67 Y. Izumi and Y. Shibata, *Chem. Lett.*, 2009, **38**, 912–913.

68 E. W. Washburn, C. J. West, C. Hull, *International critical tables of numerical data, physics, chemistry and technology, Volume VI*, National Academy of Sciences, U. S. A., International Council of Scientific Unions., National Research Council, U. S. A., 1929, pp. 242.

69 C. C. Wong, W. Chu, *Chemosphere,* 2003, **50**, 981–987.

70 K. Bouzidi, M. Chegaar, and A. Bouhemadou, *Solar Ener. Mater. Solar Cells*, 2007, **91**, 1647–1651.

71 K. Zhao, L. Zhang, J. Wang, Q. Li, W. He, and J. J. Yin, *J. Am. Chem. Soc.*, 2013, **135**, 15750–15753.

72 M. Guan, C. Xiao, J. Zhang, S. Fan, R. An, Q. Cheng, J. Xie, M. Zhou, B. Ye, and Y. Xie, *J. Am. Chem. Soc.*, 2013, **135**, 10411–10417.

73 B. Pare, B. Sarwan, and S. B. Jonnalagadda, *J. Mol. Struc.*, 2012, **1007**, 196–202.

74 M. Gellender, *J. Renewable Sustainable Energy*, 2010, **2**, 023101.

Table of contents entry

The combination of n-type TiO_2 and p-type BiOCl photooxidizing water and photoreducing formed O_2 back to water, respectively, in acidic solution enabled sustainable photofuel cell utilizing natural light.

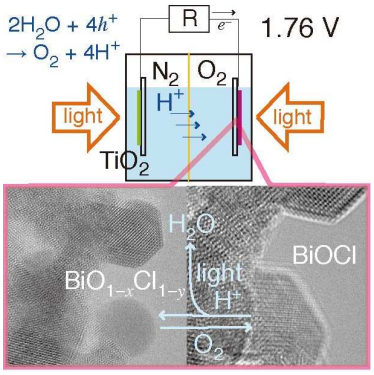

Electronic Supplementary Material

An HR-TEM video observation of BiOCl in an Ar atmosphere and irradiated under UV–visible light for 1 h is available.